"A SURVEY OF MSC/PISCES APPLICATIONS".

Written by: A.M.A. van der Heijden
P.H.L. Groenenboom

Date: February 1990

The MacNeal-Schwendler Company B.V.
Gouda, The Netherlands

Abstract.

Applications of advanced computer programs for transient analysis have for a long time mainly been restricted to defense applications and safety studies for nuclear plants. In recent years, however, applications in other industries especially, the automotive industry, have become more and more important.

In this paper a selection of problems from various industries is presented which have been solved with the family of MSC/PISCES codes. The purpose of this paper is to show that these general purpose codes enable the engineer and scientist to solve a broad class of problems with *the same tools*.

1. Introduction.

The field of highly dynamic phenomena is becoming more and more important for engineers and scientists. This is on the one hand due to the fact that many products have to satisfy higher standards, but on the other hand due the to fact that tools for the simulation of these phenomena have become available on powerful computers.

The problems to be treated with these tools are often very complex in the sense that apart from the highly dynamic behaviour, nonlinear behaviour is a rule rather than an exception. The family of MSC/PISCES codes provides the engineer and scientist with tools that can be used in a *production environment*, i.e. they have been validated, are continuously maintained and updated, and are well documented. The codes contain a library with a large number of material models, for both fluids and solids. Furthermore the user can decide which part of the problem he wants to model in Euler, Lagrange or Shells and then couple the parts with each other. This allows him for instance to carry out fully coupled fluid-structure interaction problems. Another distinct feature of these codes is that they allow for user written subroutines i.e. if the user wants a feature that is not standardly available, he can in many cases create that feature himself.

The programs all use an explicit integration technique in the time domain. For the spatial discretization the one- and two-dimensional codes use finite difference techniques, whereas in the three-dimensional codes finite element techniques are used for the discretization of the Lagrange and shell descriptions.

For the explicit time integration to be stable the time step has to satisfy the so-called Courant criterion, which for Lagrange means that the time step has to be smaller than the smallest zone length divided by the local sound speed. This means that for most problems the time step is small, say of the order of a microsecond. This explains why explicit time integration techniques are not well suited for stationary solutions. On the other hand it has been proven that for short time duration processes explicit time integration is to be favoured over implicit integration techniques.

2. A brief description of the MSC/PISCES codes.

The MSC/PISCES codes solve the conservation laws of continuum mechanics i.e.

- the conservation of mass
- the conservation of momentum
- the conservation of energy

together with constitutive equations and the equations of state. For the time integration an explicit finite difference method is used. The family of codes consists of the following programs:

PIPE : This is an Eulerian finite-difference program to compute fluid and gas flow problems of piping systems in three-dimensional space. [1]

2DELK V4 : This is a two-dimensional Euler-Lagrange coupled finite-difference program to solve dynamic structure, fluid flow or fluid-structure interaction problems. [2]

Grain-Burning : This code is based on the 2DELK V3 code, but contains a modified Euler processor for the description of a continuum model consisting of a dynamic mixture of two reactive components in two-dimensional space. [3]

3DELK*) : This is a three-dimensional Euler-Lagrange coupled finite-difference / finite-element program to solve dynamic structural, fluid flow, or fluid-structure interaction problems.[4]

---

*) *At present two versions exist:*

- 3DELK (old) : This version is an Euler-Shells coupled finite-difference / finite-element program, in which the coupling is based on a local ALE technique.
- 3DELK (new) : This program is still under development. At present Lagrange and Euler (single material, without strength) are available and the coupling between these two processors. This coupling allows for arbitrary motion of a body through the Euler grid. Furthermore rezoning of the Lagrange-grid is possible.

AIRBAG : This is a special version of 3DELK (new) which contains membranes for the description of the Airbag material and gas laws for simplified Airbag inflation calculations. [5]
This program may (on a limited number of hardware platforms) be coupled with the CVS program MADYMO, to simulate Airbag-occupant behaviour. [6]

3. MSC/PISCES applications.

The MSC/PISCES codes have been successfully applied to a large variety of problems. Most of these problems involved highly dynamic non-linear behaviour of structures and for fluids or gases. The non-linearities may be caused by a number of phenomena e.g. geometric non-linearities, material non-linearity or non-linear boundary conditions.
In a number of applications the fluid-structure interaction plays a crucial role.
The applications to be presented are from the following industries:

- *Aerospace*
- *Automotive*
- *Defense*
- *Petrochemical*
- *Power plants*

Aerospace

3.1 Atlas Centaur stage separation by shaped charge firing.

In 1984 an Atlas-Centaur launch vehicle, flight AC62, experienced an in-flight failure due to a leak in the liquid oxygen propellant (LO2) tank immediately after the firing of the stage-separation shaped charge. Numerical simulations of the shaped charge (SC) firing and of the response of the LO2 tank have been performed with PISCES-2DELK as part of the failure investigation [7]. The simulation calculation was split into an early-time model for the SC perforation of the forward adapter or ISA ring and the dynamic loading of the protective blast shield up to 100 microseconds (see figures 3.1.1 and 3.1.2) and a late-time model, driven by the early-time model, for the response of the LO2 tank up to 10 milliseconds. The SC-performance calculations were verified against ballistic pendulum tests with a series of shaped charge similar to the one use for AC62, with good agreement. The influence of the increasing size of the gap between the ISA-ring and the blast shield on the time of impact radial velocities is shown in figure 3.1.3. Parameter studies with the early-time model showed that this gap is the most important parameter determining the impact loading of the blast shield and the peak stresses in the tank skin. A comparison of the computed stress with the measured stress in the sycamore tests for AC63 conditions, with increased gap size, are shown in figure 3.1.4; those for AC62 in figure 3.1.5. The conclusion is that the peak pressure at the tank skin is reduced for the modified ISA-ring configuration. The moderately high stress is not sufficient to have caused the failure for the AC2 configuration. The fact that the peak pressure occurs at the probable AC62 failure position provides some arguments in favour of the detonation augmentation hypothesis.

Automotive

3.2 Numerical simulation of airbag behaviour.

A recent application in the automotive industry is the simulation of a deploying airbag and of an impacting object (the driver or passenger) on it [8].
Aspects of airbag behaviour such as unfolding and wrinkling, and oblique or non-central body impact are fully three-dimensional phenomena. However, parameter studies on airbag inflation, including effects of straps and holes and on normal, central impact in axial symmetry (2D) are very useful and can be performed economically and the results may be compared to most experiments.

The inflation of an axial symmetric airbag with two small holes close to the inflator and with elastic straps has been computed as a coupled Euler-shell model in PISCES-2DELK. The bag (fig. 3.2.1) is modelled by membrane elements of which the left side is fixed to the steering column. Additional constraints are posed by the attached straps and by the steering wheel. The initial shape is that of a slightly curved, flat pancake with the original surface area. At the outside atmospheric pressure is assumed. The Eulerian mesh is also shown in fig. 3.2.1. Since the part outside the bag is covered, gas is only allowed inside the bag. The gas enters from the inflator with specified density, temperature and mass flux. The holes in the zone next to the inflator opening are modelled as a narrow circumferential slit in the polygon that allows transfer from air/nitrogen through the bag; the structure of the bag itself remains intact. The computed airbag shape, flow field and material distribution after 11 and 23 milliseconds are shown in figure 3.2.2. The small regions of different material inside the bag demonstrate that air from outside the bag has flown into the bag due to the pressure drop in the flow field in front of the inflator openings. After 35 to 40 milliseconds the inflow of gas becomes very small and the bag has reached its final shape. Damping is provided by the presence of gas. The straps limit the deflection of the bag.
Airbag inflation and impact of a human body model has been simulated in a three-dimensional geometry using the PISCES-AIRBAG program coupled with the MADYMO program of TNO [6]. In this model the gas flow inside the bag has been neglected, instead a uniform internal pressure has been assumed which is determined by the current amount of inflator gas and the current volume of the bag. In a series of meshplots (figure 3.2.3) the deployment of the airbag and the impact of the drivers head and chest is shown. The presence of the steering wheel has been taken into account.
Application of subcycling techniques to save computer time will be discussed elsewhere [22].

Defense

3.3 Aerodynamic drag of tubular projectiles.

Tubular projectiles as the Solid Fuel Tubular Ramjet (SFRJ) and the Spinning Tubular Projectile (STUP) shown in fig. 3.3.1, are being used as training munitions. The range of the tubular projectiles is reduced due to the sharp increase in the drag coëfficient at decreasing Mach number. This increase is due to a transition of the flow regime from started flow to choked flow. Both regimes are shown in fig. 3.3.2 as flow visualisations obtained in a supersonic wind tunnel by Berner and Giraud [9]. The actual flow regime of a tubular projectile does not only depend on the geometry and the current Mach number but it also exhibits a hysteretic behaviour within a certain range of the flight Mach number. For a fixed inlet geometry, there exists a range of flight Mach number $M_c < M < M_s$ for which both flow modes may prevail. For $M < M_c$ the flow is always choked (with a detached bow shock), whereas for $M > M_s$ the flow is always started, with a supersonic flow throughout. Upon acceleration, the bow shock will not be swallowed until M_s is reached. Once swallowed, however, the shock will not be expelled upon deceleration until M_c is reached.

A computational analysis using the second order Euler processor of PISCES-2DELK for ideal gas neglecting viscosity, has been carried out by Y. Kivity [10]. Two types of initial conditions have been applied: for the first one the air is quiscent and at uniform pressure and temperature, for the second one velocity, pressure and temperature of a shock are assumed in the internal part of the projectile, simulating gun firing conditions (fig. 3.3.3). The velocity vector plot and pressure contour plot of figure 3.3.4 for the uniform initial conditions show all relevant features of started flow, whereas the flow for the calculation starting with gun firing initial conditions (fig. 3.3.5) is in the choked mode. In fig. 3.3.6, the computed pressure distributions for M = 2.06 and M = 3.02 may be compared to the experimental results of Berner and Giraud [9]. There is qualitative agreement with the measured values, with good agreement near the inlet. The difference with the measured values for the lower Mach number might be attributed to the fact that the computational results have not fully converged after 2600 cycles.

The main conclusions are that the computed flow mode for the transition range of the flight Mach number depends on the initial conditions, corresponding to the hysteresis effect, and that the inviscid flow calculations seem to be adequate to predict the main features.

3.4 Explosively Formed Projectiles.

The PISCES-2DELK code has been applied to projectiles which are formed if a warhead hits a target; these explosively formed projectiles (EFP's) are designed to penetrate a thick wall of armor. A sketch of an EFP charge of OTO Melara [11] is given in figure 3.4.1. The charge consists of a detonator, an explosive booster, the main explosive, i.e. COMP B in a cylinder, and a 35 mm thick metal sheet, the liner, which will be shaped into a projectile by the explosion. The corresponding computational model is shown in figure 3.4.2; the explosive is described in the Eulerian grid which extends in all directions to allow for the expected expansion. The liner and other structural part not shown in figure 3.4.2, are modelled as Lagrangian grids. The interaction is provided by the available polygon logic. The propagation of the detonation wave for the programmed explosive burn logic is shown in figure 3.4.3. The development of the liner into the final projectile shape is shown in figure 3.4.4. The effect of the behaviour of the liner material at high strains, high strain rates and elevated temperatures on the final shape and velocity may be studied. According to Pezzica [11] good agreement with the measured velocity and with the final shape as found by X-ray photography may be obtained using proper material models (see fig. 3.4.5).

3.5 Impact and penetration.

The PISCES-2DELK code has been validated for several high velocity impact and penetration problems. The first example is the computation of the impact of a long cylindrical rod made of tungsten at 3700 m/s on a thick wall of Rolled Homogeneous Armour (RHA) steel [12]. At this impact velocity the rod will penetrate the target as though it were a fluid jet impinging on a large body of fluid. It is important that the strength of both materials is described accurately including strain-and strain rate hardening and thermal softening. Since large plastic deformations may be expected, not only the rod is modelled in an Euler subgrid but also the part of the target in which the crater will be formed is Eulerian (fig. 3.5.1). These Euler grids are joined so that the rod material moves into the target grid. The remaining part of the target model is described in a Lagrangian grid. For the interaction between the Eulerian part and the Lagrangian part of the target a polygon with infinite friction and cohesion is defined; this prevents unphysical sliding or separation of both parts. The proceeding phases of the penetration and cratering process may be observed in figures 3.5.2. The final shape of the crater is compared to the shape measured by Charters [13] (see fig. 3.5.3). The computed depth of 7.31 cm is 6% less than the experimental value. This result is excellent considering the inaccuracy in the test results and in the tungsten material data [12, 13].

The second example is the penetration and perforation of a tungsten carbide projectile on a 20 mm thick armoured steel target. The configuration is shown in figure 3.5.4 together with the X-ray photographs of the damage for a range of impact velocities. The computation has been performed with Lagrangian subgrids for both projectile and target using the impact logic [14]. The initial mesh layout is shown in figure 3.5.5. A number of rezones have been performed in the target subgrid to cope with the strong deformations in the parts of the target where material failure occurred. The final configuration of figure 3.5.6 shows that the projectile perforates with a plug of target material at the nose. From the remaining kinetic energy it may be deduced that the ballistic limit is 518 m/s which is only 1.8 % less than the value of 528 m/s interpolated from the experiments. It may be concluded that with limited engineering effort and negligible computing effort, even with this coarse mesh good agreement with experimental results has been achieved.

A third example is the impact of a tungsten steel projectile on ceramic armour. The impact velocity is about 760 m/s. The armour consists of a ceramic layer with a thickness of 8.12 mm and an aluminum backing layer with a thickness of 6.4 mm.
The results of this simulation shown in figure 3.5.7 illustrate the main feature of the accompanying penetration phenomenon:

- the development of a fracture conoid initiating at the impact surface and spreading inwards
- the initiation of cracks on the axis at the boundary between the ceramic layer and the backing layer (due to tensile stresses)
- pulverization of the ceramic
- flattening of the projectile nose

All this happens before the projectile starts to penetrate the ceramic. The simulation shows that most of the kinetic energy and momentum of the projectile is lost during the penetration of the ceramic. Part of the loss of kinetic energy and momentum of the projectile is due to erosion of the projectile.

Defense

3.6 Response of a raft to an underwater explosion.

PISCES-2DELK has been used to compute the response of a raft structure to a close range underwater explosion of which a test has been carried out at N.S.W.C., White Oak [15]. The test raft structure is topped with several layers of steel plate sandwiched with energy absorption foam. These steel plates are supported by a steel grid box that is partitioned into several compartments. The box is filled with air. The raft structure floats on a pond of water. The pond is deep enough so that the response is not complicated by the reflection of the pressure wave from the pond boundary within the period of interest. A cylinder of High Explosive (HE) is placed in the water directly underneath the raft structure at the center. Velocity response at the top of the raft structure is measured.
Although the actual problem is three-dimensional, a reasonable axi-symmetric model may be defined [15].
The important phenomena that are simulated include the detonation of the HE, the expansion of the explosive product in the water, interaction of the plate structure with the highly compressed water and air, destruction of the steel plates, venting of the explosive product through the enlarging holes, impact effect between the plates, and compaction of the energy absorption foam. All of these phenomena are important to the final results.

The HE, water, and the air are modeled in an Euler grid, the steel plates are modeled with shell grids, and the energy absorption foam is modeled in a Lagrange grid. JWL (see reference 16) equation of state is used to simulate the behaviour of the HE, and the Herrmann P-alpha model (see reference 17) is used to model hydrodynamic compaction of the foam.

Figures 3.6.1 through 3.6.4 depict the complex phenomena at four different times, 0.14 ms, 0.55 ms, 0.86 ms, and 1.3 ms. During the early stage, very fine zoning surrounding the HE is required to accurately track the propagation of the shock wave generated from the explosion. The velocity vectors approximately define the wave front in the water and air (inside the box). The Euler grid is expanded and rezoned as the HE product and shock wave expand (Fig. 3.6.2). Destruction of the bottom plate and its impact on the layered plates is shown in figures 3.6.2, 3.6.3 and 3.6.4. Also the expansion and diffraction of the HE, the destruction of the box structure, and the deformation of the layered plates can be observed. PISCES-2DELK calculations with fine zoning cases compared quite well with several scale tests. Deviation from the experiments for these cases range from 2 percent to 10 percent.

Defense

3.7 Two examples of simulations of a regenerative test device.

Together with Rheinmetall GmbH, a number of calculations were performed to simulate various processes relevant to liquid propellant gun propulsion with a regenerative test device. The results of these calculations were first presented at the Ballistics Symposium in Brussels [18].

Figure 3.7.1 shows the model of a regenerative test device. The presence of the igniter and also the injection orifices in the piston disturb the rotational symmetry. Another disturbance of this symmetry may be caused by a gas bubble that may form in the liquid reservoir.
We shall briefly discuss two simulations:

i) The collaps of a gas bubble in the liquid reservoir.
ii) Injection process and the flow through the piston.

ad i) Consider a gas bubble in the liquid reservoir (see fig. 3.7.2). The size of the bubble is 5 by 18 mm. The behaviour of such a bubble under a pressure load is one of the important questions in the theory of liquid propellants. The presence of such bubbles may lead to unsafe conditions. Let a pressure pulse of 700 MPa run through the liquid form the left to the right. This pressure pulse will then pass the bubble and interact with it, leading to a peak pressure of 1.5 GPa (see fig. 3.7.3).
Such pressures may lead to detonation of the liquid. The pressure distribution after reflection from the outer wall is shown in fig. 3.7.4.

ad ii) The piston has two rows of holes. Making use of the symmetry of the problem, only a wedge has to be considered for this simulation (see fig. 3.7.5). The top part of this figure shows the Euler grid, the bottom part the Lagrange grid. The pressure difference between the liquid in the reservoir and the combustion chamber is about 110 MPa, which causes the injection of liquid from the reservoir into the combustion chamber. The figures 3.7.6 show the density distribution of the liquid at two different times during the injection process.

Defense

3.8 Two phase reactive flow in a granular propellant gun.

The interior ballistics of a granular propellant gun may be studied numerically with the Grain-burning option of PISCES-2DELK. This special version Euler processor describes a mixture of incompressible particles and compressible fluid including transfer of mass, momentum and energy due to combustion, drag and heat transfer. Ignition and burning of the granular propellant bed and acceleration of a projectile has been computed for the BOFORS 40 mm gun [19]. A drawing of the very similar, 30 mm model gun has been included as figure 3.8.1. The axial-symmetric mesh is given in figure 3.8.2; note that the barrel (shown only partly) is initially covered by the projectile. The propellant consists of small cylindrical particles with a central perforation and with or without coating. The burn rate and released combustion enthalpy vary during burning. The ignition is started by inflow of hot gas in axial direction. Drag between propellant and gas, and between the projectile and the barrel are taken into account.

Time histories of the computed pressure at two locations in the combustion chamber are shown in figure 3.8.3; these may be compared to the measured pressure histories at the corresponding transducer positions (fig. 3.8.4). There is a very good agreement between the computed and measured pressures. The computed projectile exit velocity of 1058 m/s is 5 percent higher than the measured exit velocity of 1005 m/s; in view of the uncertainty in the projectile friction this result is quite satisfactory. Additional results are given by Groenenboom and Thomson [19].

Chemical

3.9 Blast wave loading of a flexible storage tank.

An example of the use of PISCES-3DELK with the coupling between Euler and Shells for the Petro Chemical industry is presented below. A storage tank of 55 meter diameter and at internal overpressure of 40 millibar is loaded by a prescribed blast wave. This blast wave is assumed to have originated by the deflagration of a gas cloud at a large distance. Due to symmetry with respect to the vertical plane in the explosion direction only one half of the geometry needs to be modelled. A cut-away view of the computational model is shown in figure 3.9.1. The structural mechanics effects of stiffeners and other internal tank structures are simulated by locally equivalent thickness and strength of the tank wall shell elements.
Pressure contours after 400 milliseconds are shown in the cut-away view in figure 3.9.2; the corresponding pressure profiles are displayed in figure 3.9.3. The deformed shape of the tank (exaggerated displacements) at the same time are shown in figure 3.9.4. Time histories of forces, moments and displacements at all relevant locations of the tank wall have been computed for further customer analysis.

Power plants

3.10 Simulation of explosions in oil-insulated electrical equipment.

An interesting study on arc-induced explosions in oil-insulated electrical equipment has been conducted at the Research Institute of Hydro Quebec [20].
The problem may be characterized as follows:
Insulation breakdown at high current levels inside the equipment may lead to the formation of an electrical arc which creates enough heat to cause oil decomposition into gas. This leads to a pressure build up which may lead to rupture of the tank.
Depending on the distance from the arc to the surface the following three rupture modes have been characterized (see fig. 3.10.1):

i) "The oil piston" i.e. the surface of the oil moves upwards and remains practically plane. This occurs when the arc is sufficiently far from the oil surface.
ii) "The domed surface" i.e. the surface of the oil moves upwards and takes on the shape of a dome. This occurs at a closer distance of the arc to the surface.
iii) "Surface breakthrough" which means the gas bubble breaks through the surface of the oil. This occurs when the arc is sufficiently close to the oil surface.

The phenomena were simulated at Hydro Quebec with 2DELK for a cylindrical container where the arc's position is on the axis of rotation. The arc was modelled in a user's routine. The results were reported at the PISCES Seminar for Advanced Users [21]. The figures 3.10.2 show that these phenomena can be reproduced with a numerical simulation.

Concluding remarks.

The examples show that a very broad class of highly dynamic phenomena can be treated with the same tools.

References.

1) "PIPE Manual".

2) "2DV4 Manual".

3) "Grainburning Manual".

4) "3DELK Manual (old)", input directives 3DELK (new).

5) "Airbag Manual".

6) J.J. Nieboer, J. Wismans and E. Fraterman "Status of the MADYMO 2D Airbag Model".
32nd Stapp Car Crash Conference, October 1988, Atlanta.

7) S. Hancock, D. Davidson, J. Gordon, P. Chao, N. Viste and J. Weber, "Numerical simulation of Atlas-Centaur Stage-separation shaped charge firing and structural response", 56th Schock and Vibration Symposium, Monterey, CA, 1985.

8) A.M.A. van der Heijden, A.J. Buijk and P.H.L. Groenenboom, "Numerical simulation of airbag behaviour", presented at SUSI, July 11-13, 1989 Cambridge, MA.

9) C. Berner and M. Giraud, "Supersonic wind tunnel investigation of a tubular projectile", Proceedings of the 11th International Symposium on Ballistics, Brussels, May 1989.

10) Y. Kivity, "On the wave drag of tubular projectiles", 40th annual meeting of the Aeroballistic Range Association, September 1989, Paris.

11) G. Pezzica, "EFP formatting modeling", PISCES seminar for Advanced Users, Gouda, November 1989 (unpublished).

References. (cont'd)

12) H. Lenselink, "Validation of the PISCES-2DELK Version 4 code for high velocity impact and penetration problems", PISCES International Technical Note, TN-87.28, 1987 (unpublished).

13) A.C. Charter, "The Penetration of Rolled Homogeneous Armor by Continuous and Segmented Rods at High Velocity": Theory and Experiments.
General Research Corporation, Santa Barbara, Report CR-86-1031
Defense Advanced Research Projects Agency DARPA Order no. 5070.

14) H. van de Graaf, "Application of impact logic and rezoning techniques for simulation of penetration phenomena performed with the PISCES-2DELK Version 4 level 28 code", PISCES International Technical Note, TN-90.02, 1990 (unpublished).

15) F.H. Chang, P. Van Gulick, J.P. Meeker, "PISCES Applications in hypervelocity penetration and underwater explosion", Proceedings of the 10th International Symposium on Ballistics, San Diego, 1987.

16) B.M. Dobratz, LLNL Explosives Handbook, "Properties of Chemical Explosives and Explosion Simulants", Lawrence Livermore National Laboratory, 1981.

17) W. Herrmann, "Constitutive Equation for the Dynamic Compaction of Ductile Porous Materials", J. Applied Physics, Vol 40, 1969.

18) U. Steffens, R. Rittel, H. Lenselink and C. Florie, "Applications of a three-dimensional gasdynamic simulation model to interior ballistics". Proceedings 11th International Symposium of Ballistics, Brussels, Belgium, May 9-11, 1989.

19) P.H.L. Groenenboom and P. Thomson, "Two phase flow computation for a 40 mm granular propellant gun in comparison with experimental results". Proceedings of the 11th International Symposium on Ballistics, Brussels, May 1989.

20) M. Foata, M. Iordanescu and C. Hardy, "Computational methods for the analysis of explosions in oil-insulated electrical equipment".
1987 Power Industry Computer Application Conference, - PICA 1987, Montreal, Quebec, Canada.

21) M. Foata, M. Iordanescu and C. Hardy, "Computational methods for the analysis of explosions in oil-insulated electrical equipment".
PISCES Seminar for Advanced Users, Gouda, November 1989 (unpublished).

22) W.E.M. Bruijs, A.J. Buijk, P.J.A. de Coo and A.A.H.J. Sauren, "Subcycling applied to the inflation of an automotive Airbag". International Conference on Dynamics, Vibration and Control, Beijing, 1990.

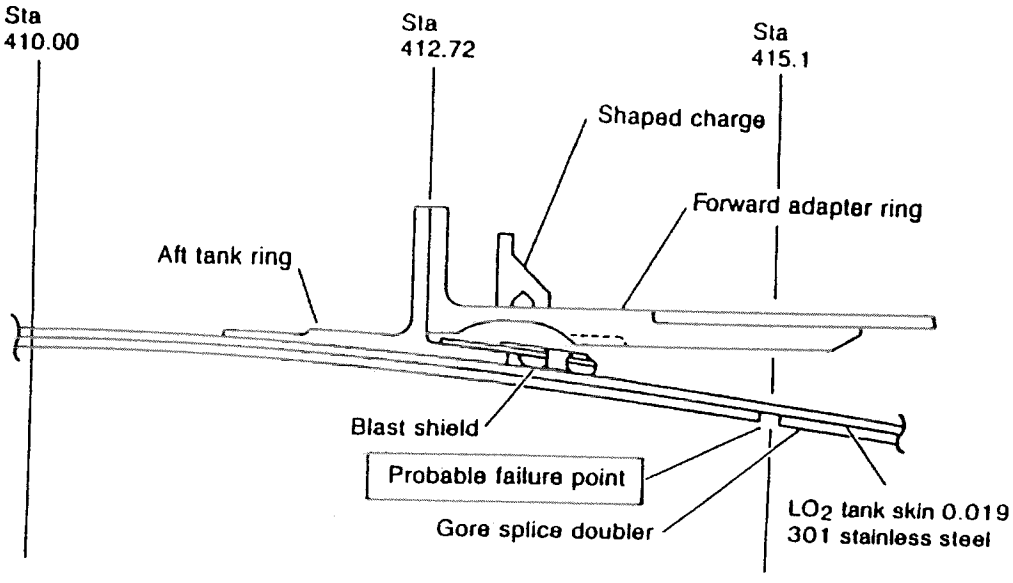

Fig. 3.1.1 Shaped charge stage separation system.

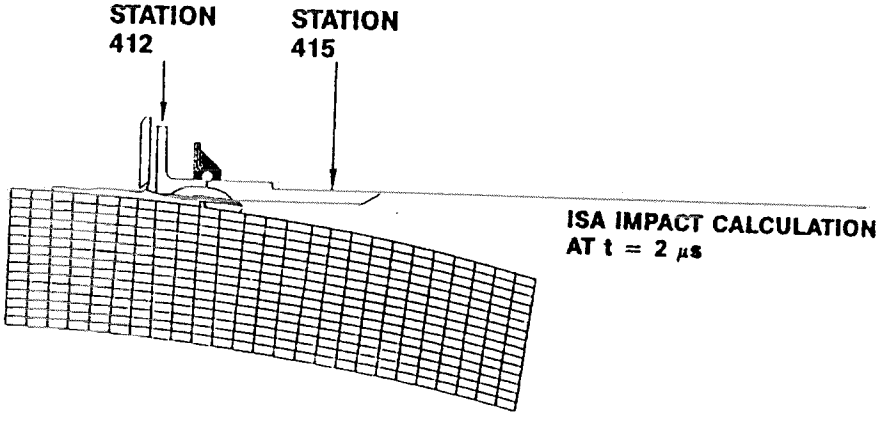

Fig. 3.1.2 Global view of the computational meshes in the calculations.

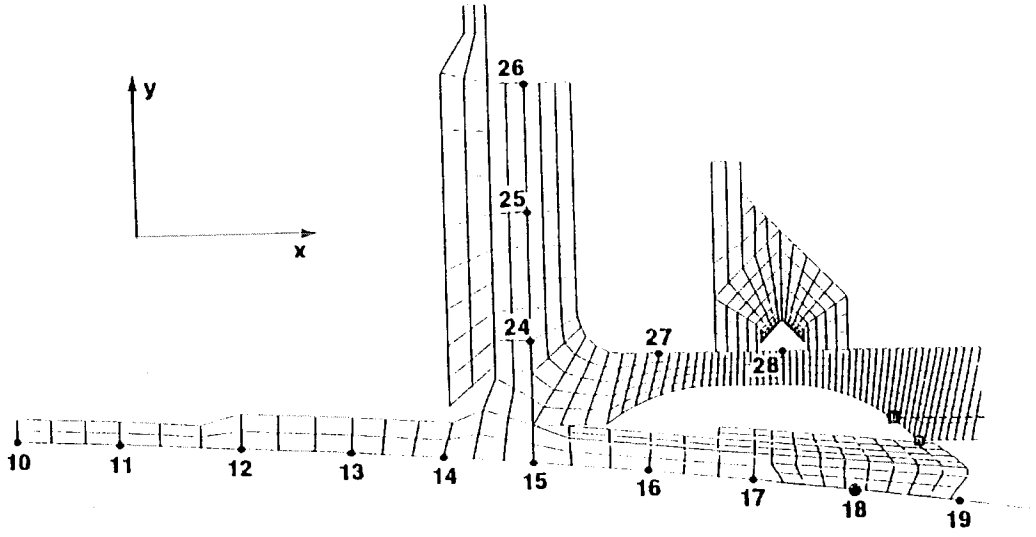

Fig. 3.1.3a Measuring points for ISA ring and undercut ring calculations (squares).

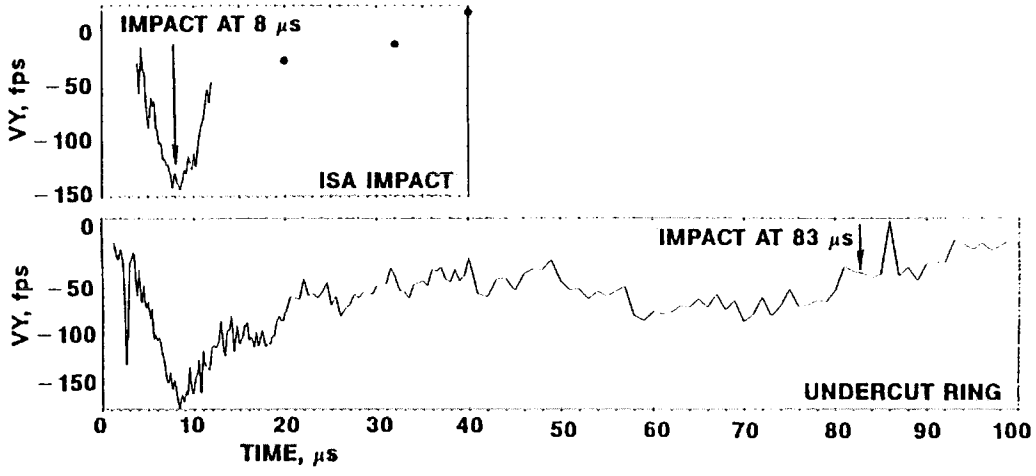

Fig. 3.1.3b Radial velocities of the point on the aft part of the ISA ring (squares in fig. 3.1.3a). After 12 μs only the discrete values indicated by the dots were obtained from the ISA impact calculations.

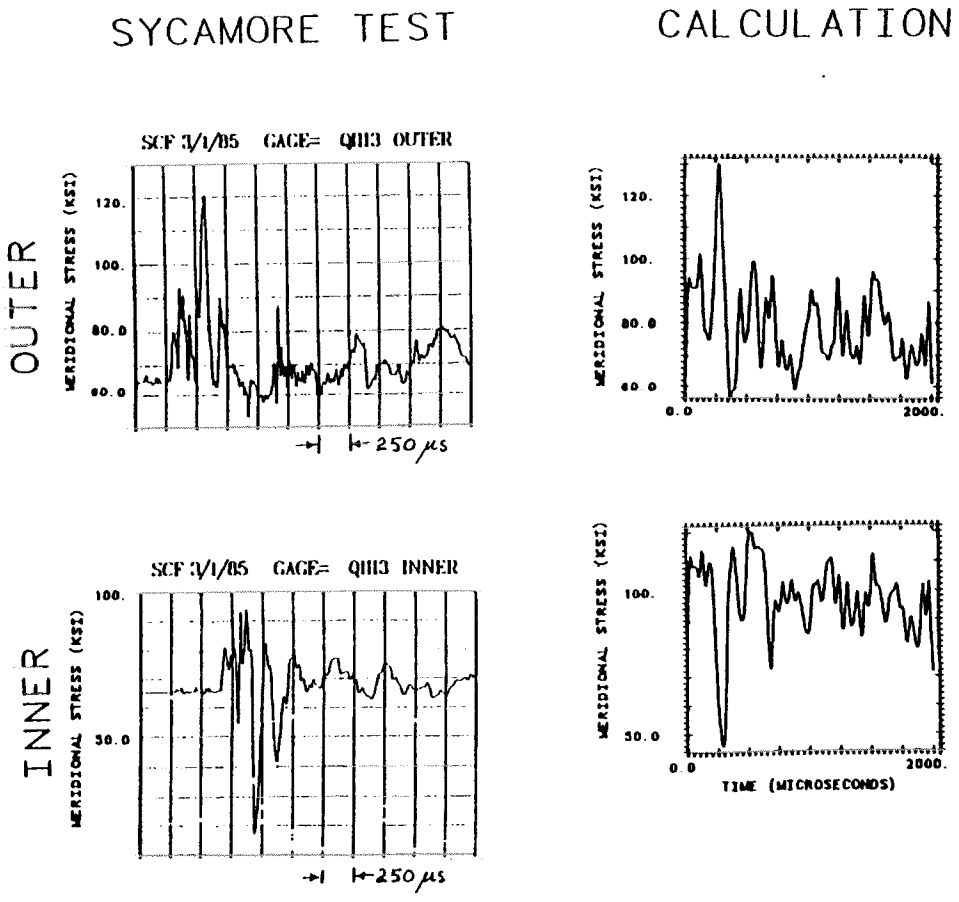

Fig. 3.1.4 Comparison of meridional stress at gage 3 for AC63 conditions.

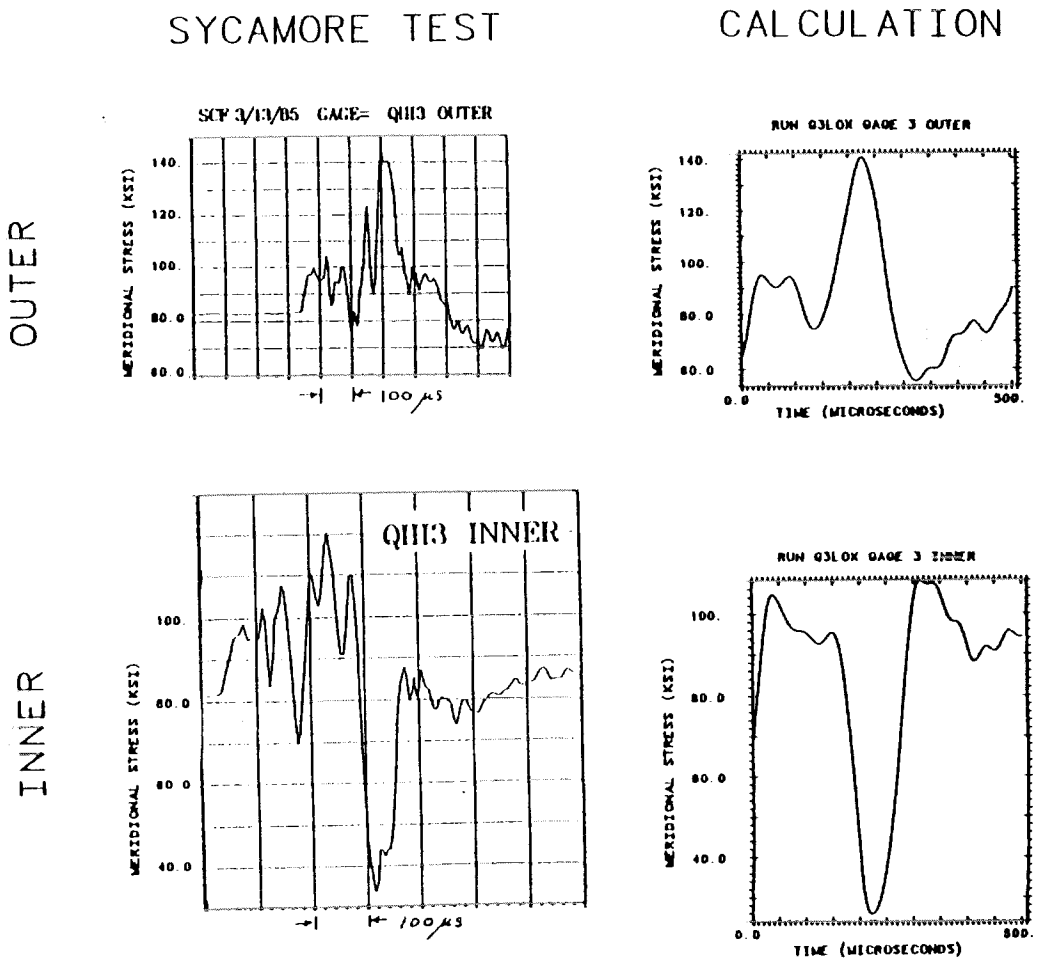

Fig. 3.1.5 Comparison of meridional stress at gage 3 for AC62 conditions.

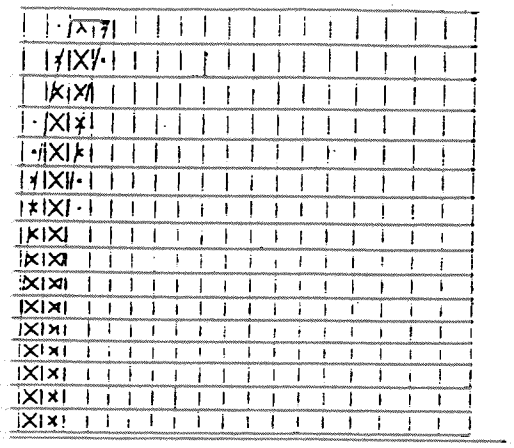

Fig. 3.2.1 Initial shape of the bag and the Euler grid.

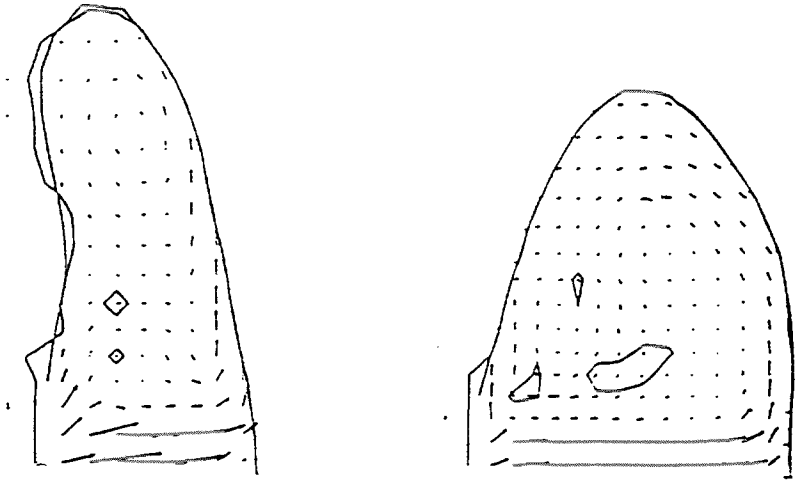

Fig. 3.2.2 Situation after 11 ms (left) and 23 ms (right).

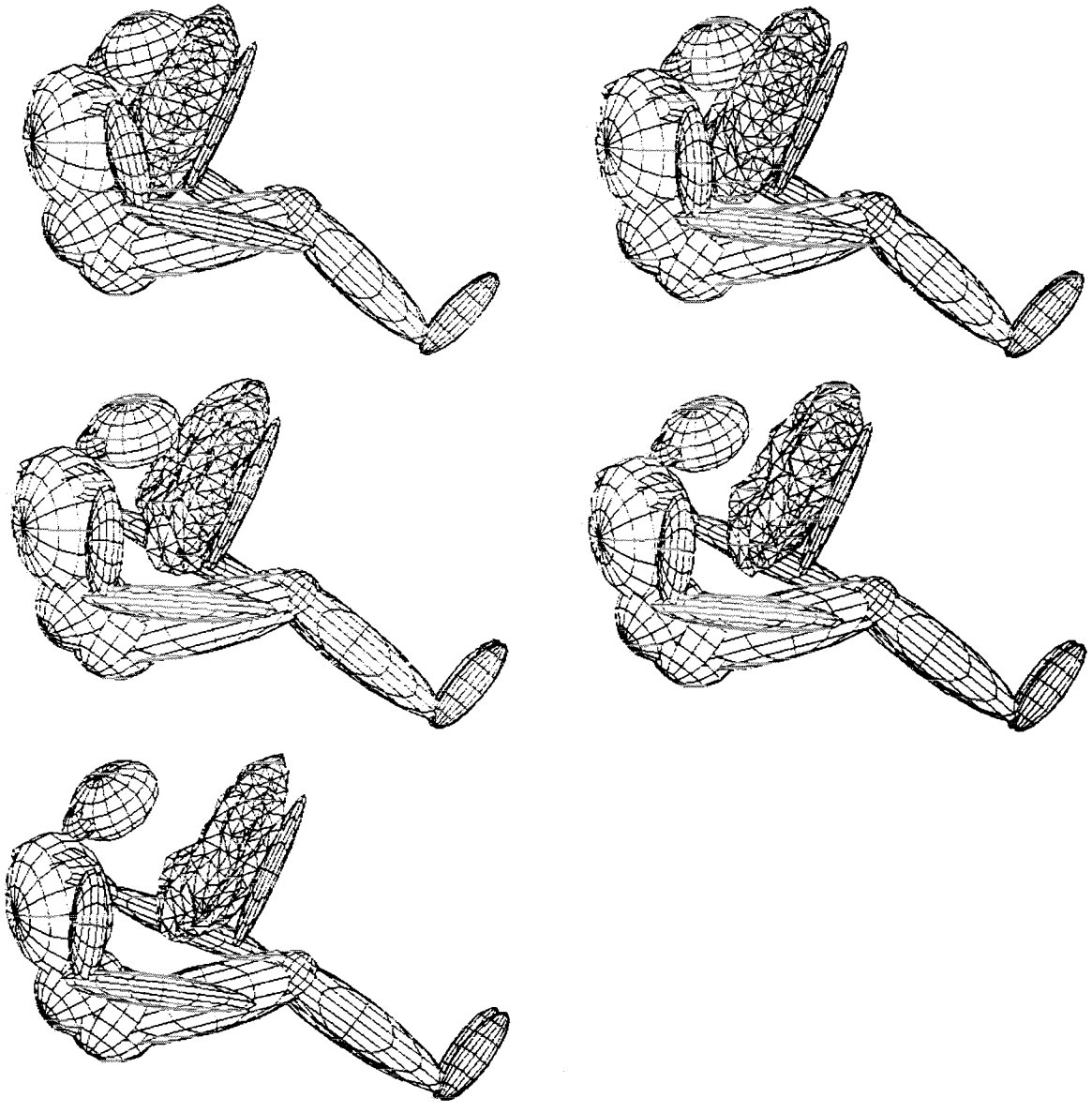

Fig. 3.2.2 Coupled AIRBAG-MADYMO calculations (continued).

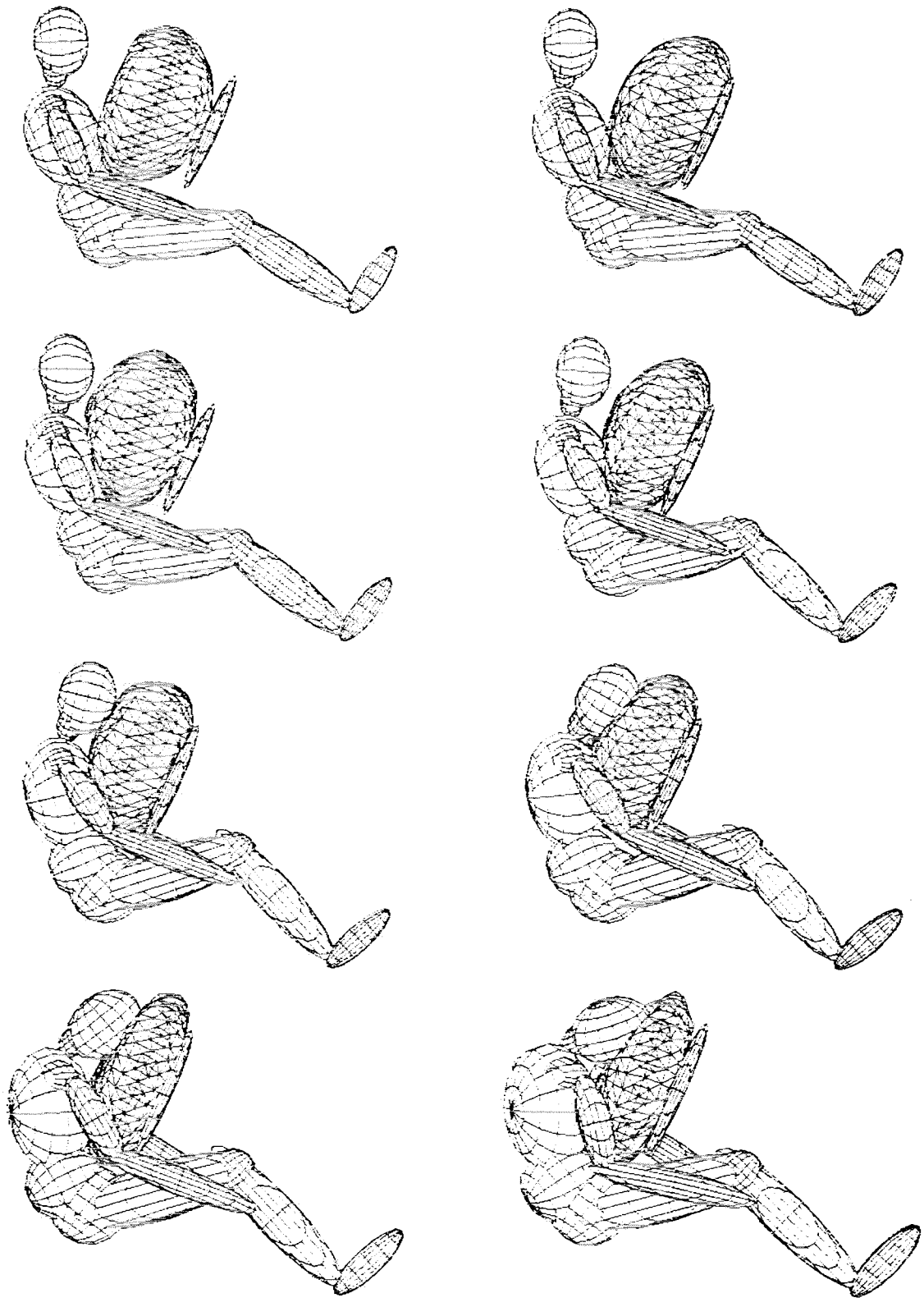

Fig. 3.2.2 Coupled AIRBAG-MADYMO calculations.

- Solid Fuel Tubular Ramjet (SFRJ)

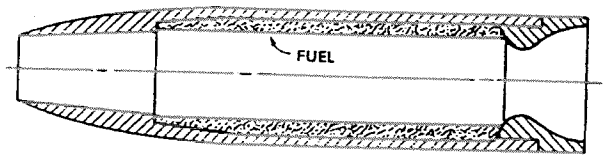

- Spinning Tubular Projectile (STUP)

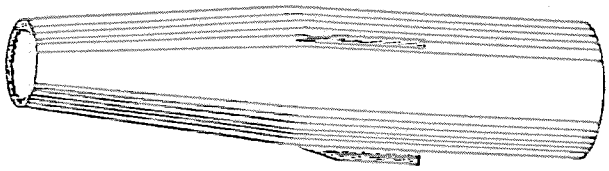

Fig. 3.3.1 Two types of tubular projectiles.

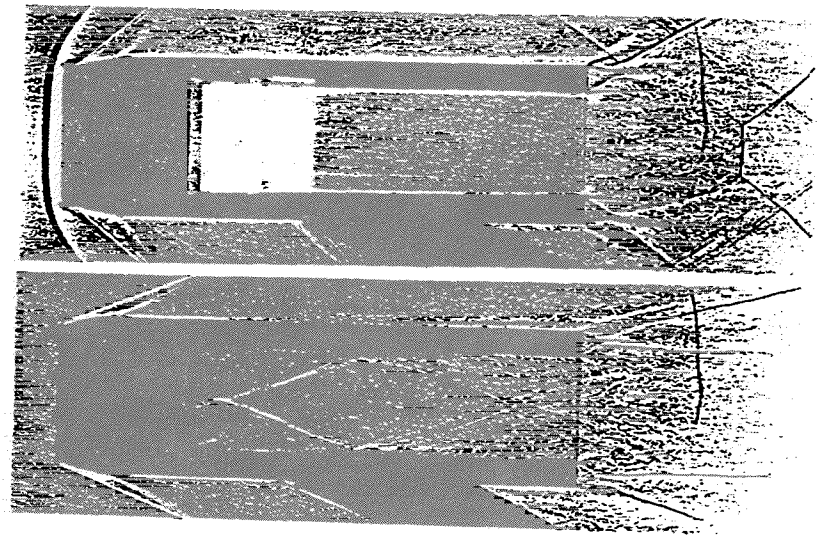

Fig. 3.3.2 Flow visualisations in a supersonic wind tunnel.

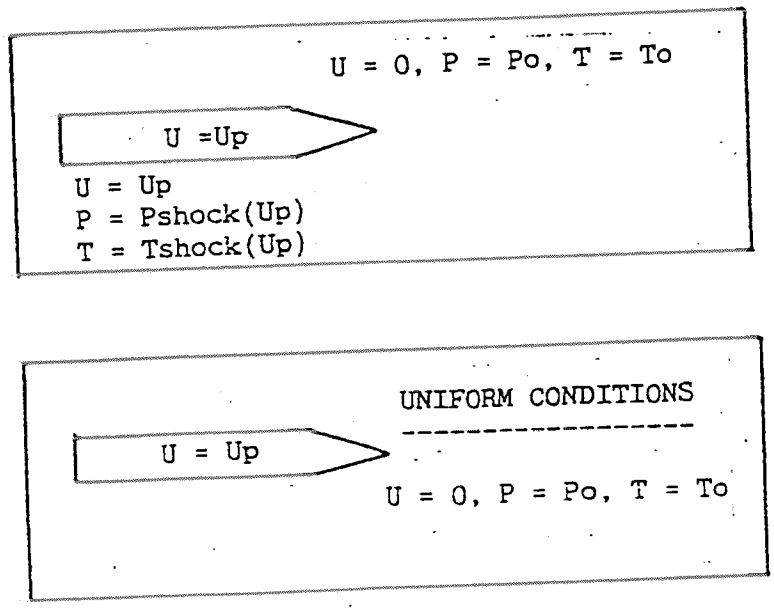

Fig. 3.3.3 Two types of initial conditions.

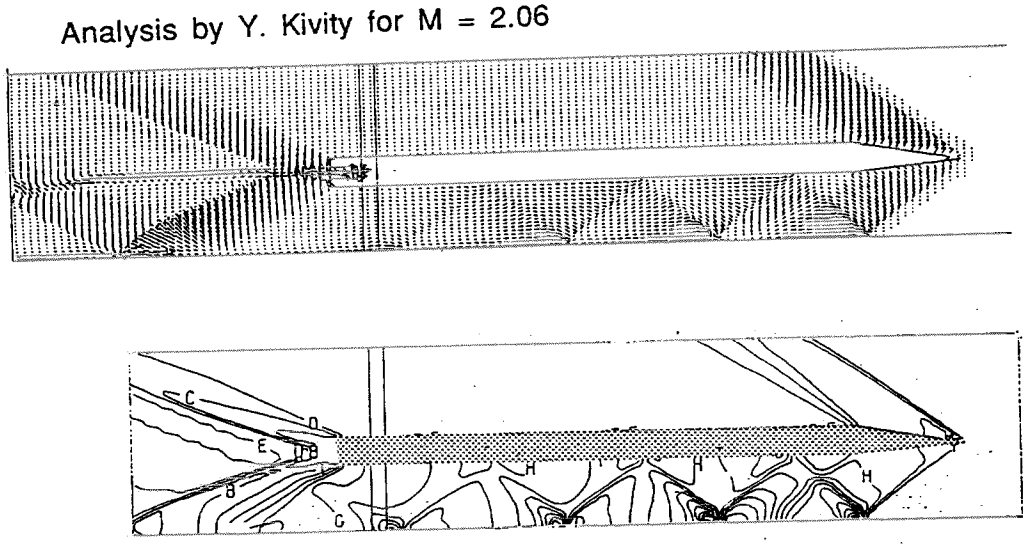

Fig. 3.3.4 Velocity and pressure field for uniform initial conditions.

Analysis of Y. Kivity for M = 2.06.

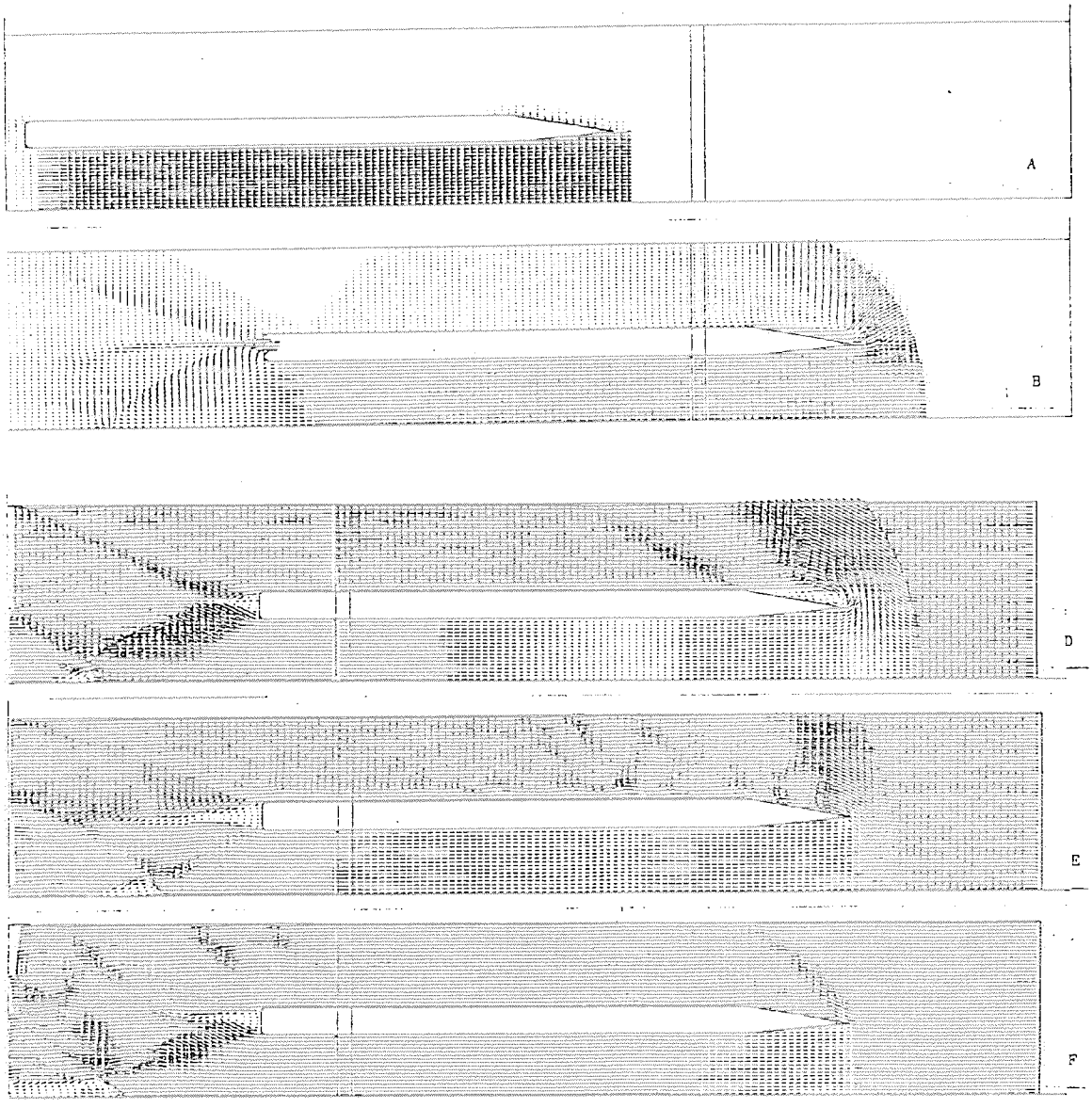

Fig. 3.3.5 Velocity fields for firing initial conditions.
D : time = 0.24 ms, E : time = 0.5 ms, F : time = 0.7 ms

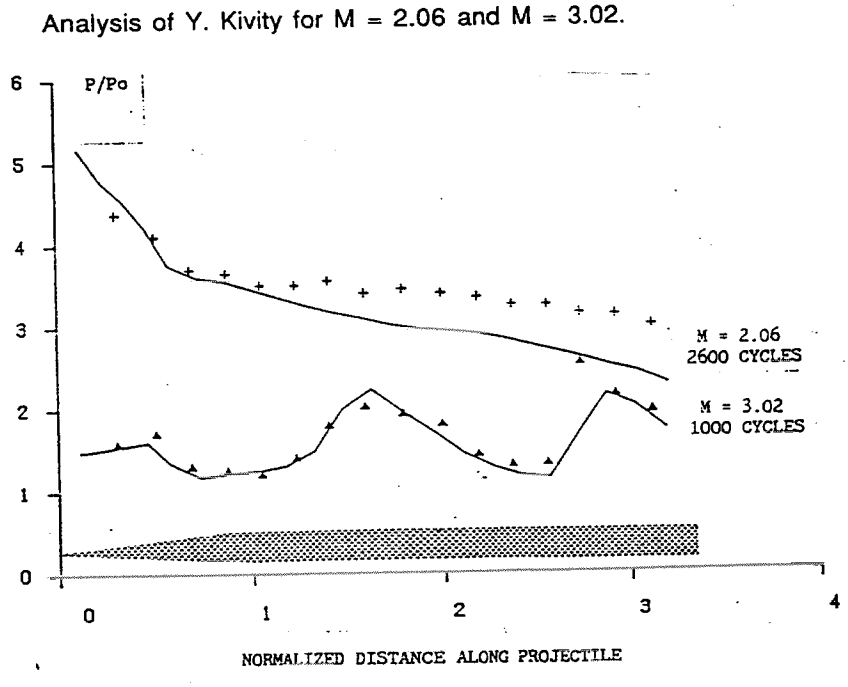

Fig. 3.3.6 Pressure distributions along the internal surface. Points represent the measurements of reference (9). Curves are the present unsteady flow calculations.

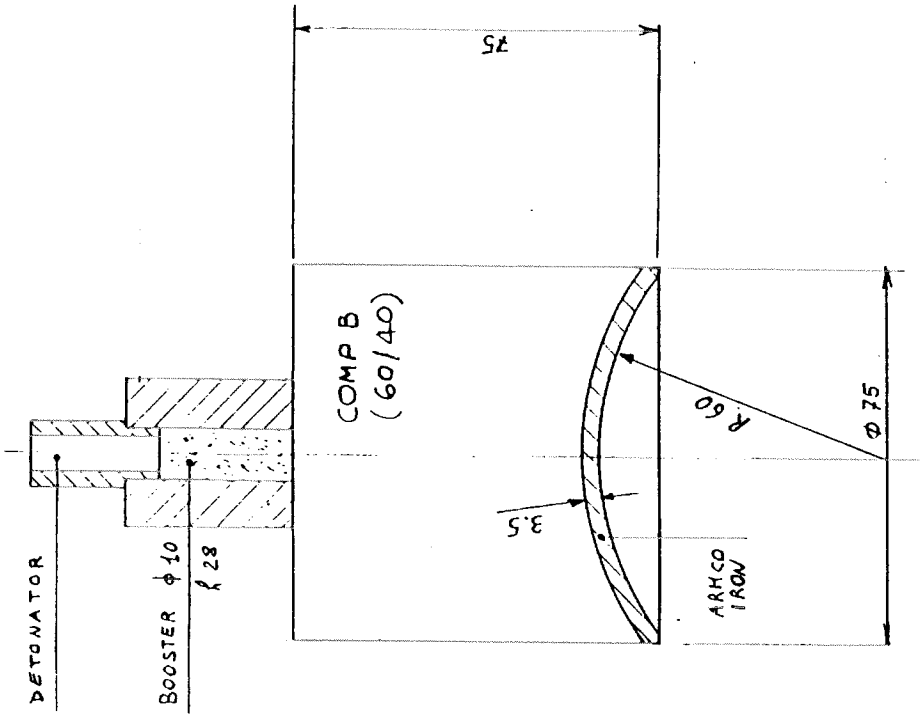

Fig. 3.4.1 Investigated E.F.P. charge.

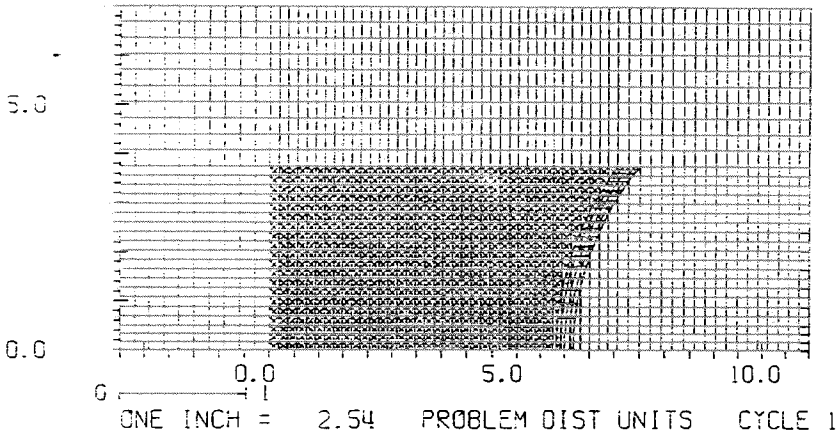

LINER : LAGRANGIAN GRID
MIE-GRUENEISEN E.O.S.
JOHNSON-COOK CONSTITUTIVE MODEL

EXPLOSIVE : EULERIAN GRID
J.W.L. E.O.S.

Fig. 3.4.2 Computational model.

H.E. DETONATION LOGIC

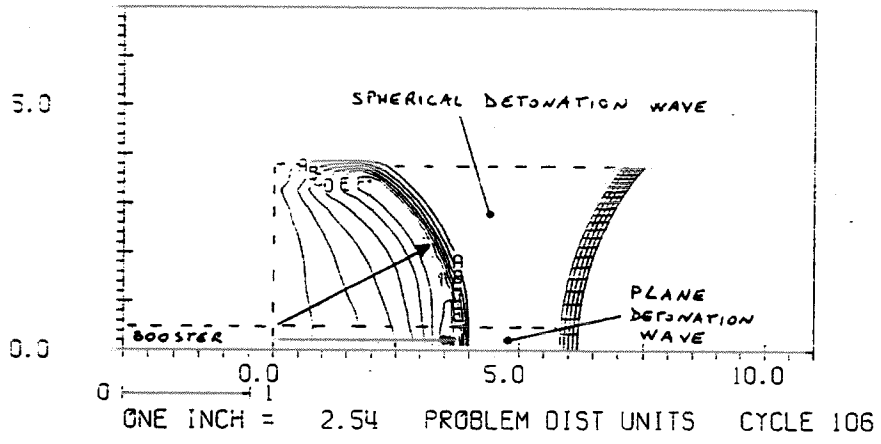

ON-TIME CRITERION FOR BURNING

Fig. 3.4.3 Propagation of detonation wave.

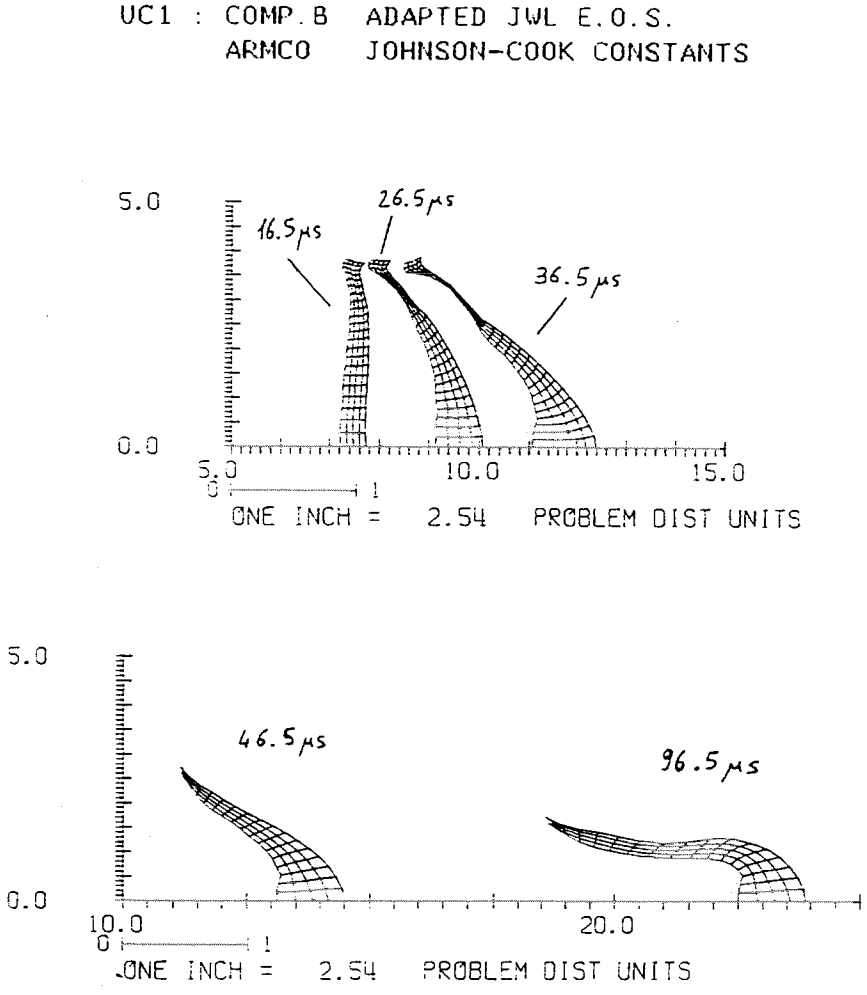

Fig. 3.4.4 Development of final shape of the projectile.

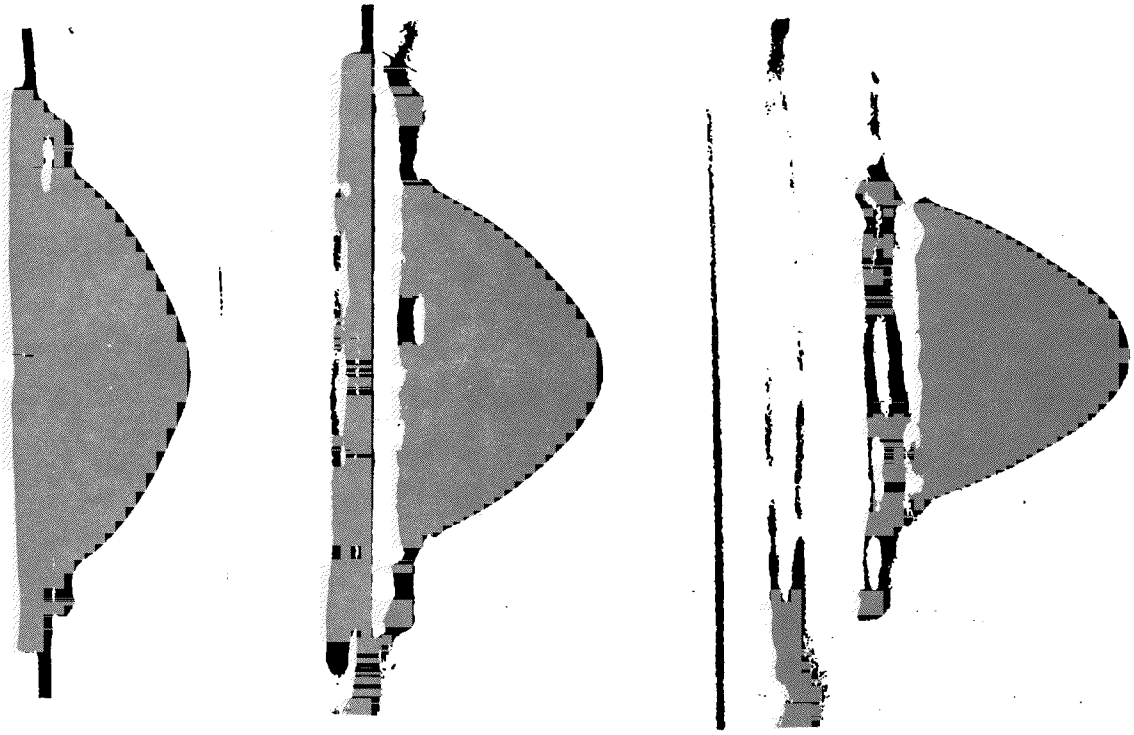

t = 26.5 μs t = 35.5 μs t = 46.5 μs

Fig. 3.4.5 Experimental data.

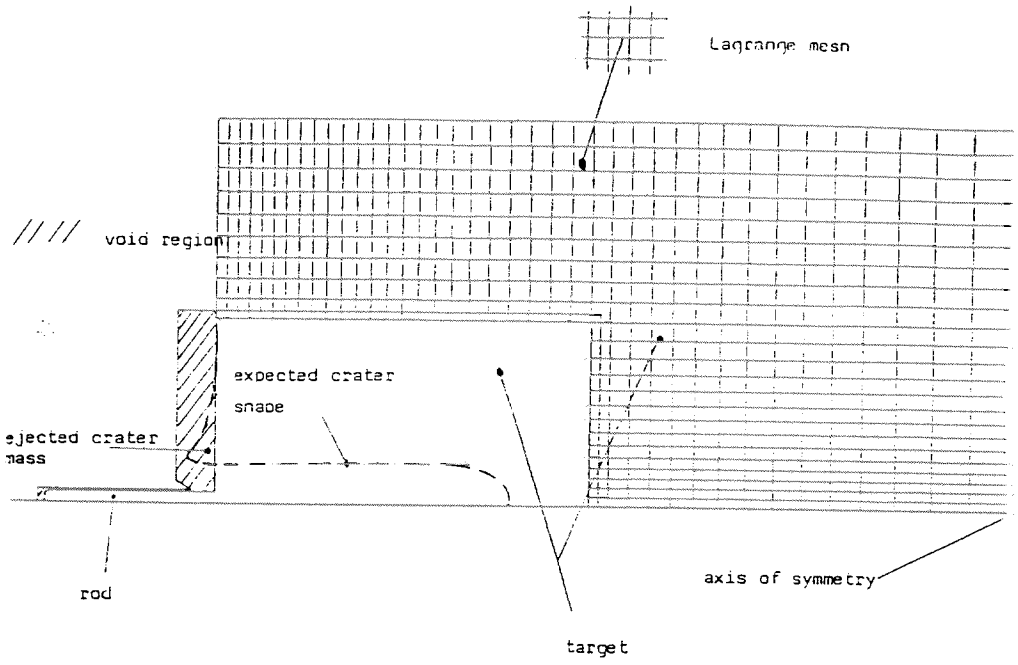

Fig. 3.5.1a Setup of the mesh.

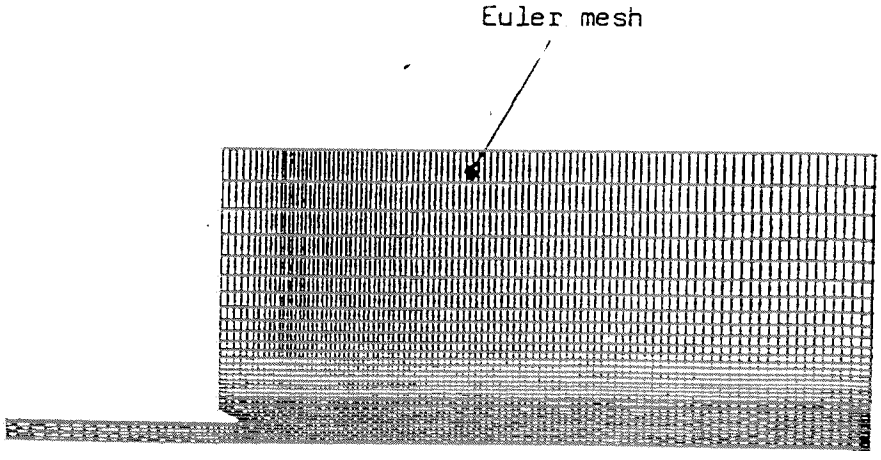

Fig. 3.5.1b The Euler mesh.

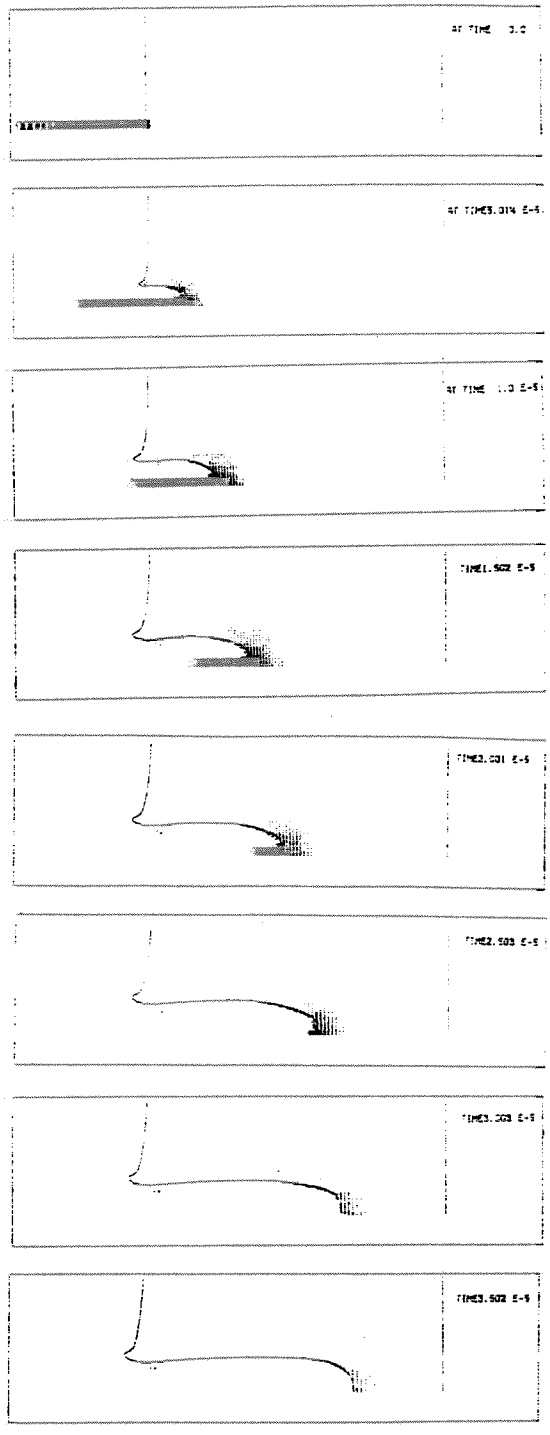

Fig. 3.5.2 The penetration process.

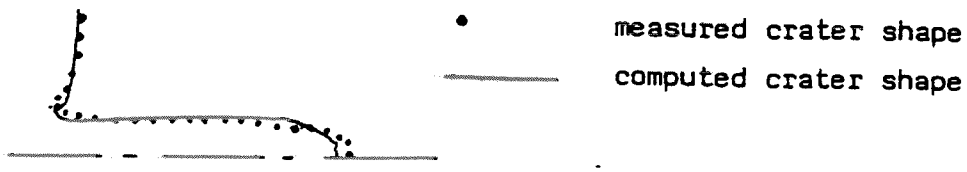

Fig. 3.5.3 Comparison of computed and measure crater shape.

1 - GEOMETRICAL CONFIGURATION IN mm OF NORMAL OBLIQUITY IMPACT BETWEEN A TUNGSTEN CARBIDE PROJECTILE CORE AND A 23 CND 8 ARMOURED STEEL TARGET.

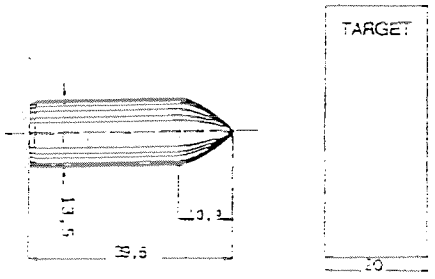

2 - STATIC MECHANICAL CHARACTERISTICS OF THE TARGET

- Density = 7,85
- YOUNG modulus = 206 GPa
- POISSON modulus = 0,3
- Yield strength = 1091 MPa
- Tensile strength = 1221 MPa
- Hardening relation = $\sigma = 1444\ \varepsilon^{0,042}$

3 - MACROPHOTOGRAPHY ASPECTS OF DAMAGE AFTER FIRING TESTS VERSUS IMPACT VELOCITY (magnification x 1).

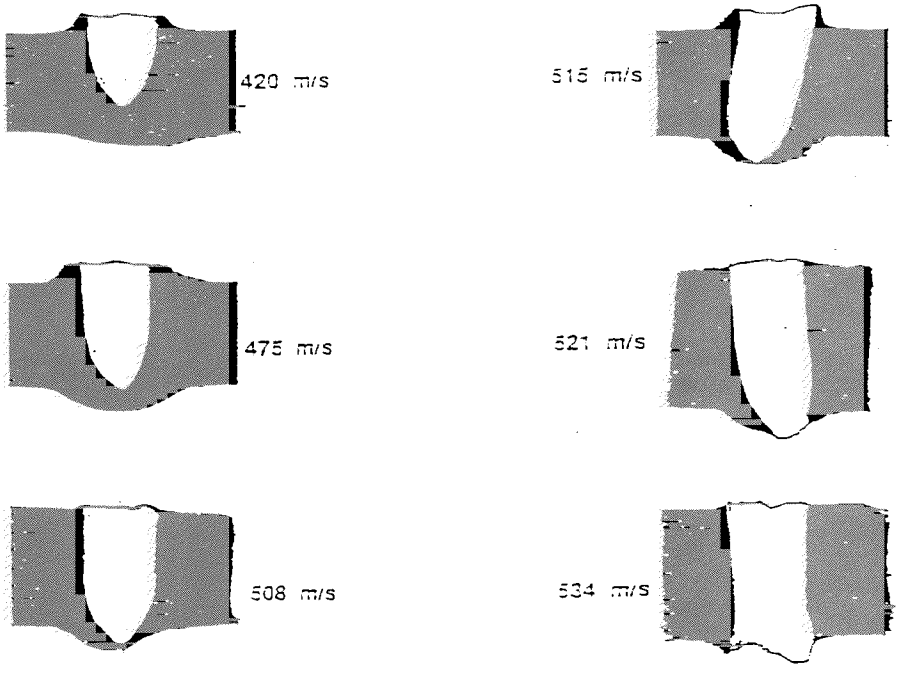

VELOCITY LIMIT OF PROTECTION = 528 m/s

Fig. 3.5.4 Penetration of an armoured steel target.

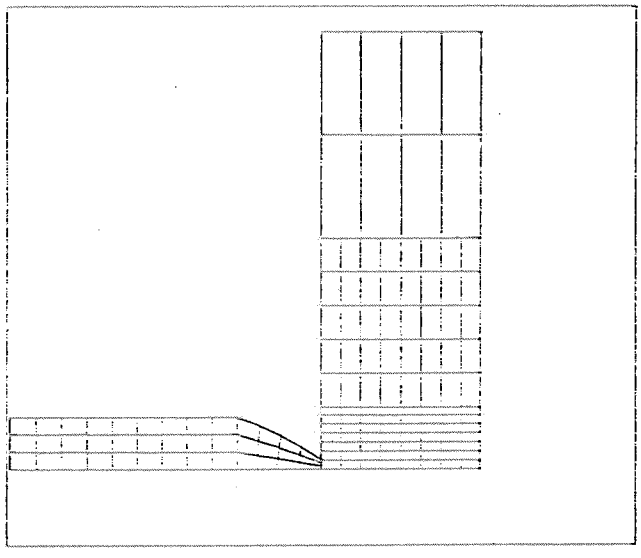

Fig. 3.5.5 Initial configuration.

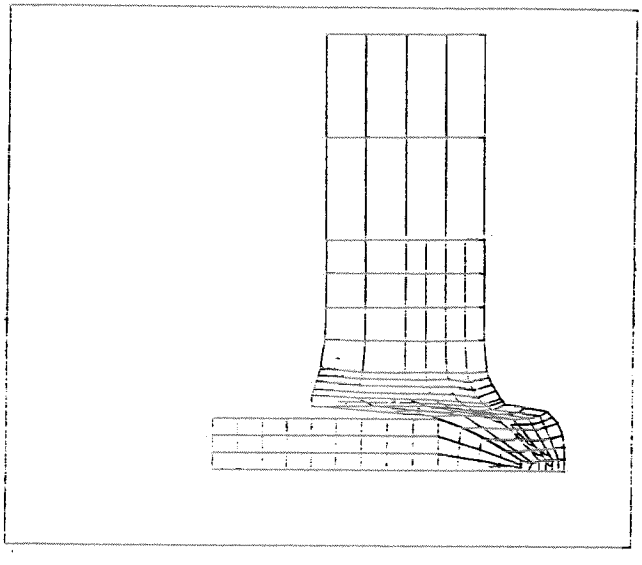

Fig. 3.5.6 Final configuration.

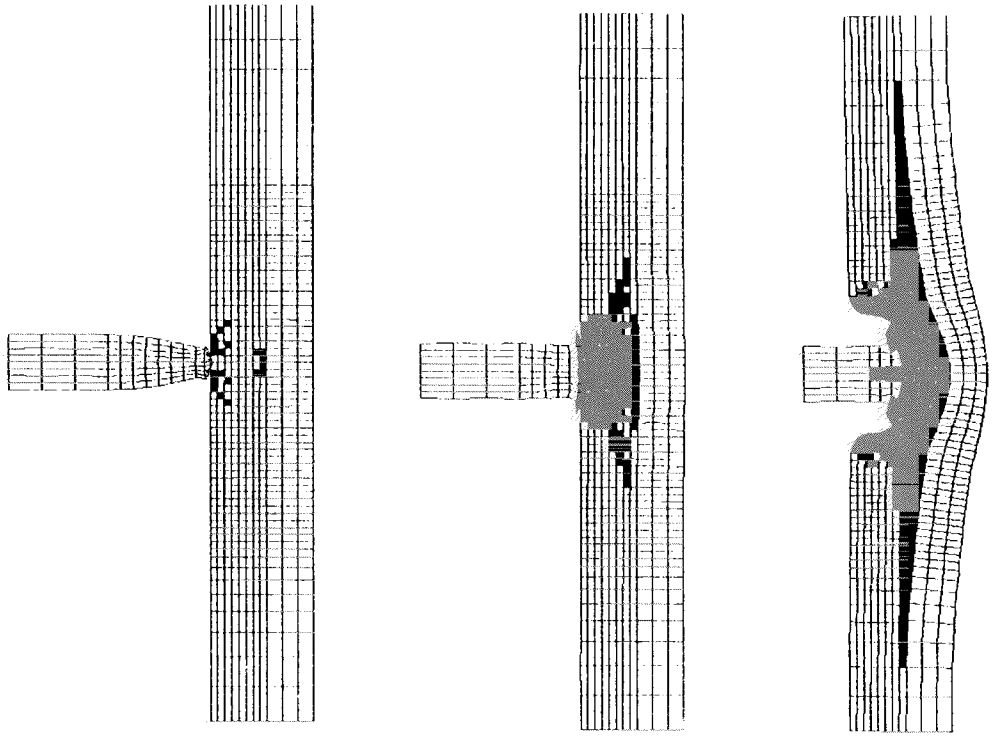

Fig. 3.5.7 Penetration of ceramic armour.

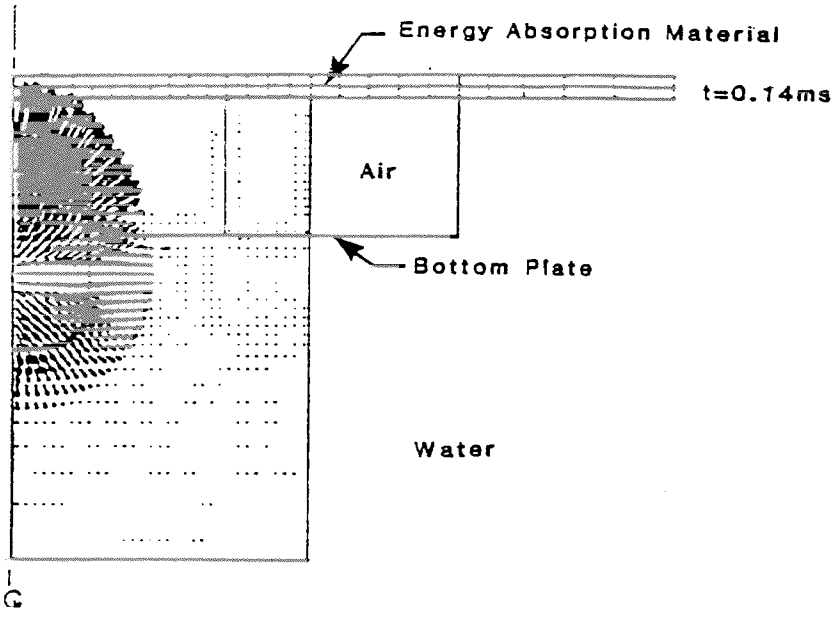

Fig. 3.6.1 Very fine zoning for the initial stage of HE expansion.

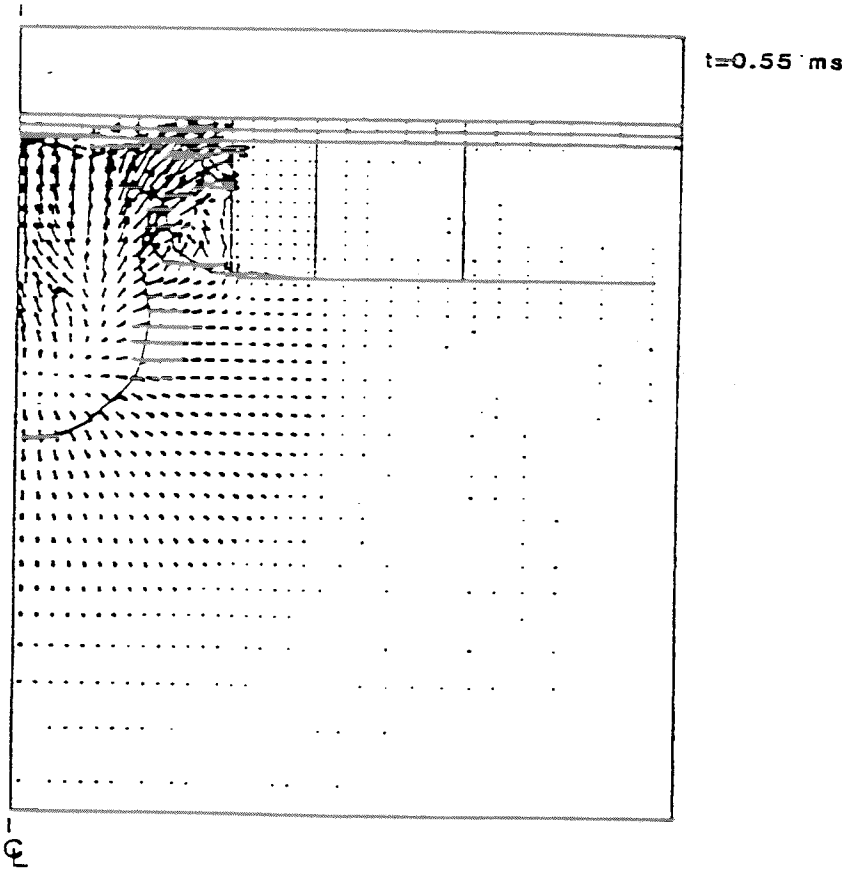

Fig. 3.6.2 Euler grid is expanded and rezoned.

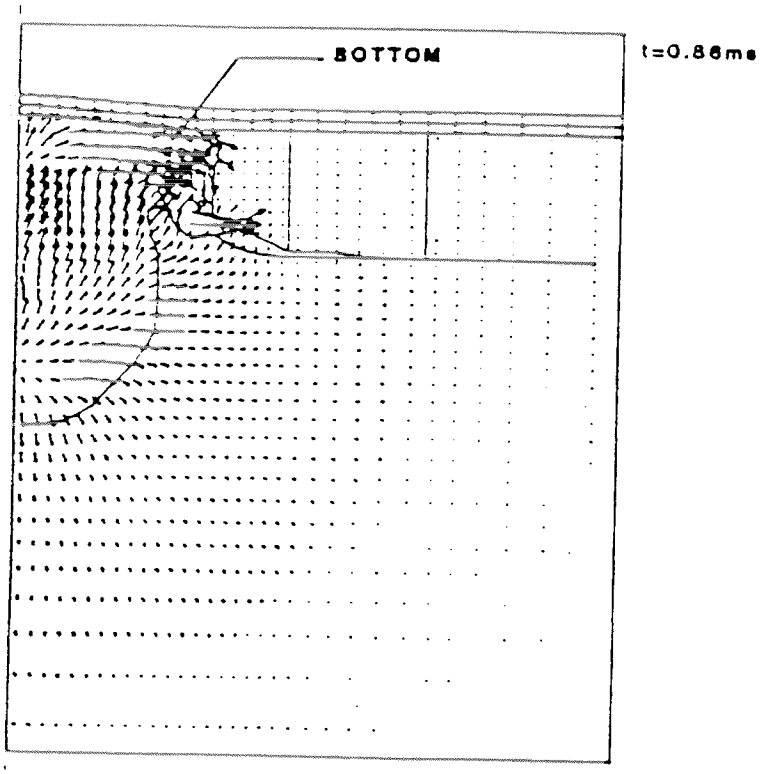

Fig. 3.6.3 Velocity vector plot at t = 0.86 ms.

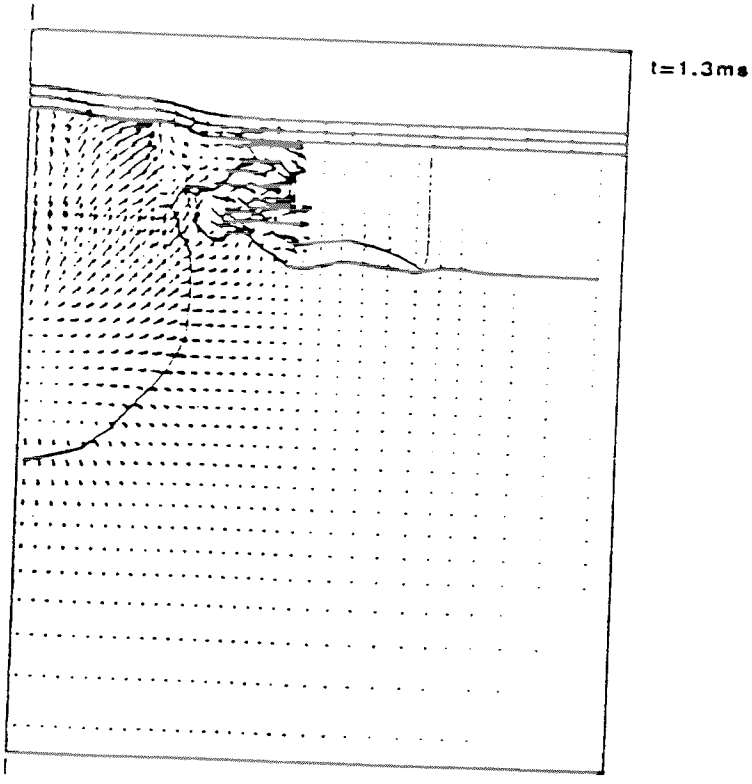

Fig. 3.6.4 Velocity vector plot at t = 1.3 ms.

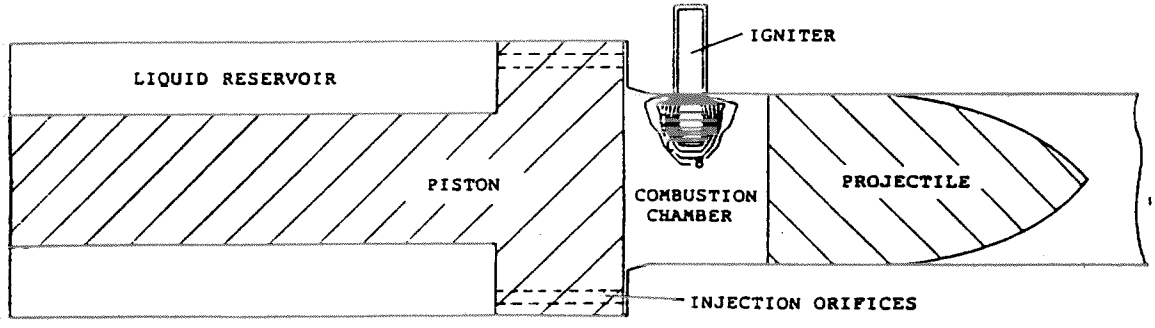

Fig. 3.7.1 Schematic of the 40 mm Inline Piston, Regenerative test device.

direction of pressure pulse.

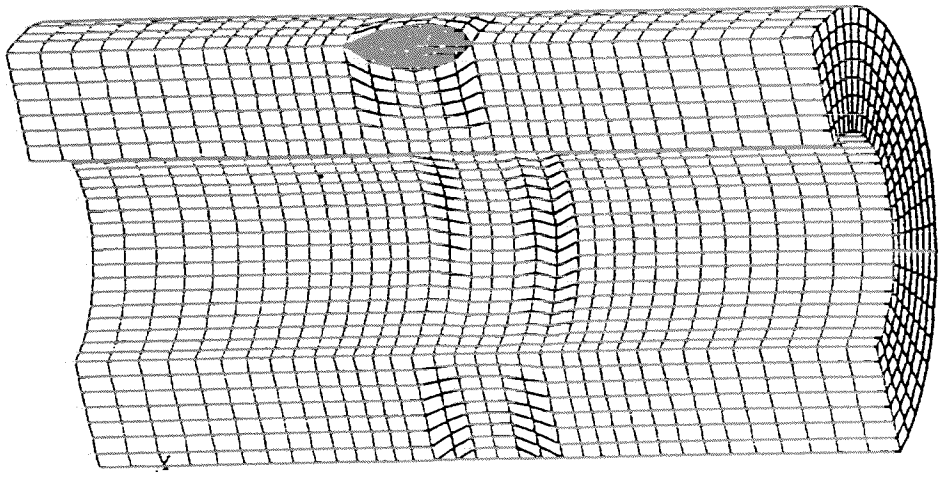

Fig. 3.7.2 Initial configuration.

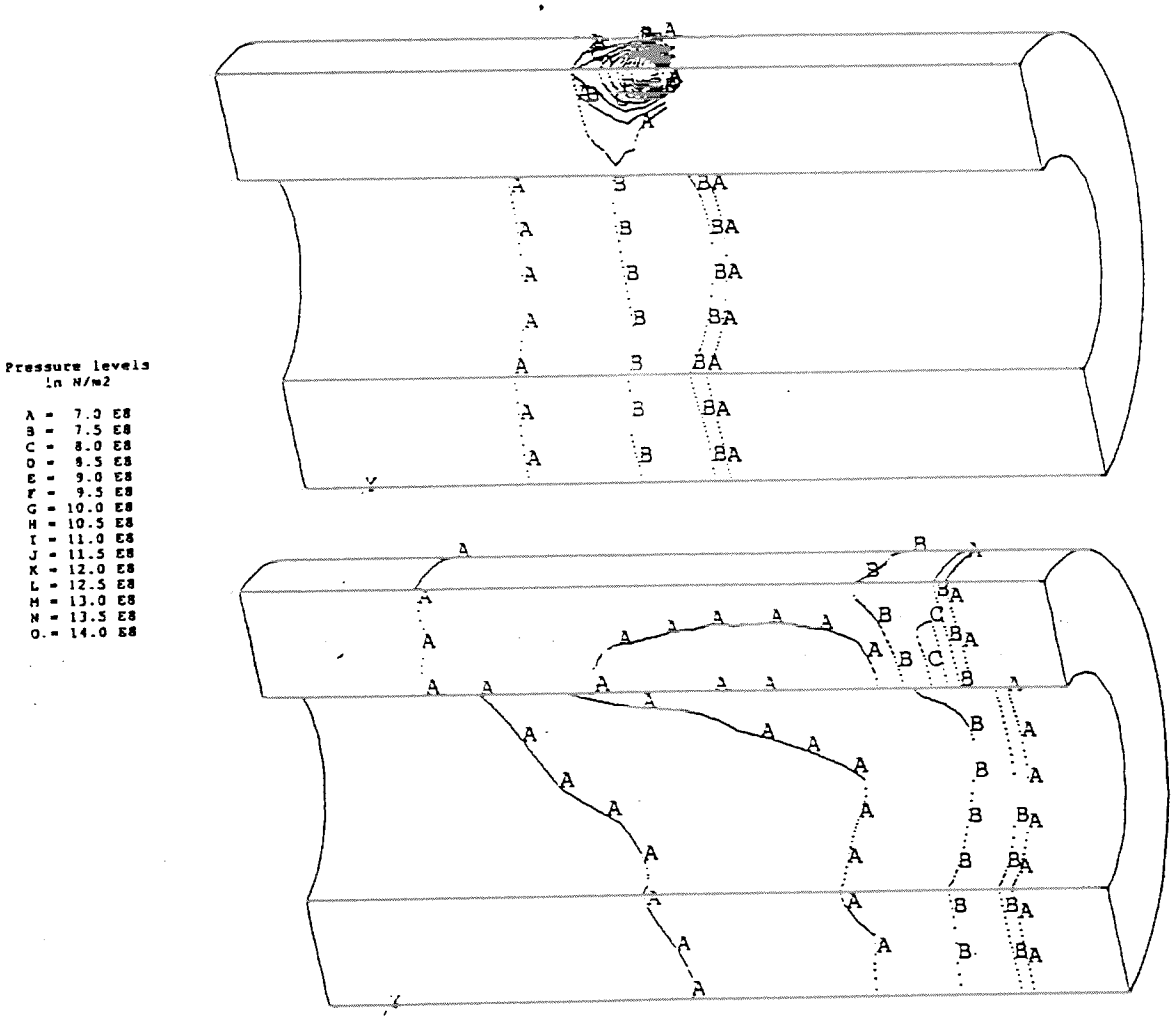

Fig. 3.7.3 Interaction of pressure pulse and gasbubble.

Fig. 3.7.4 Pressure distribution after reflection from outer wall.

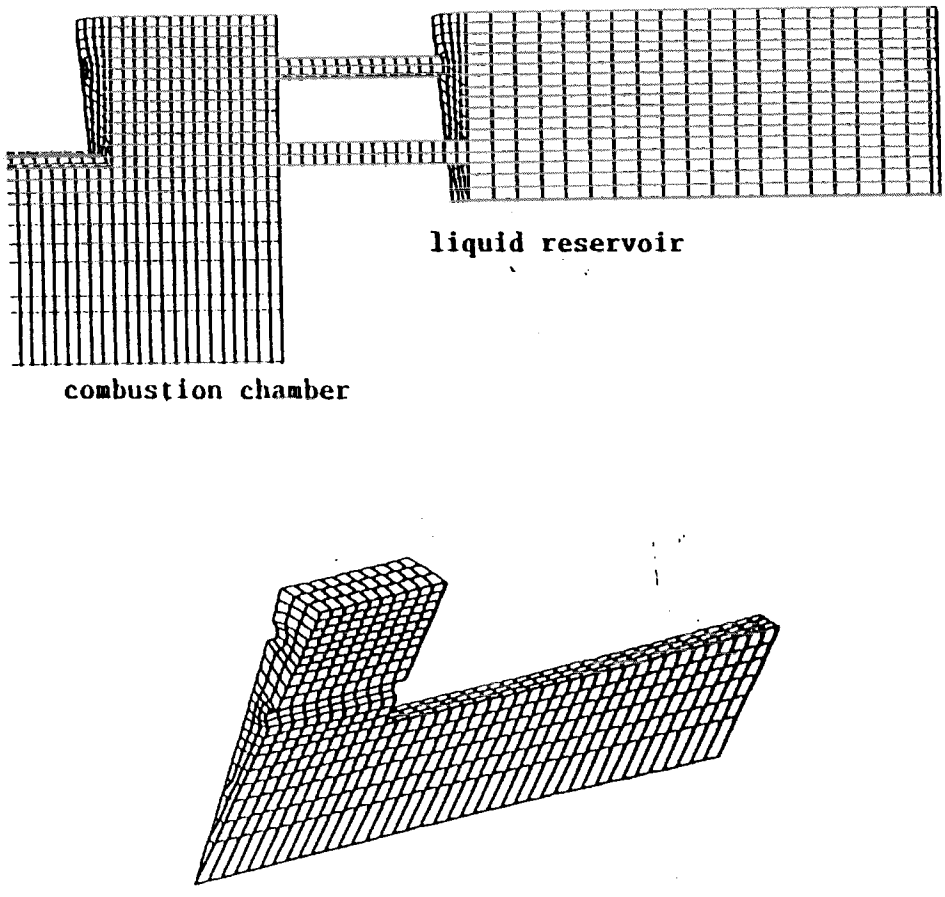

Fig. 3.7.5 The Euler grid (top) and the Lagrange grid (bottom).

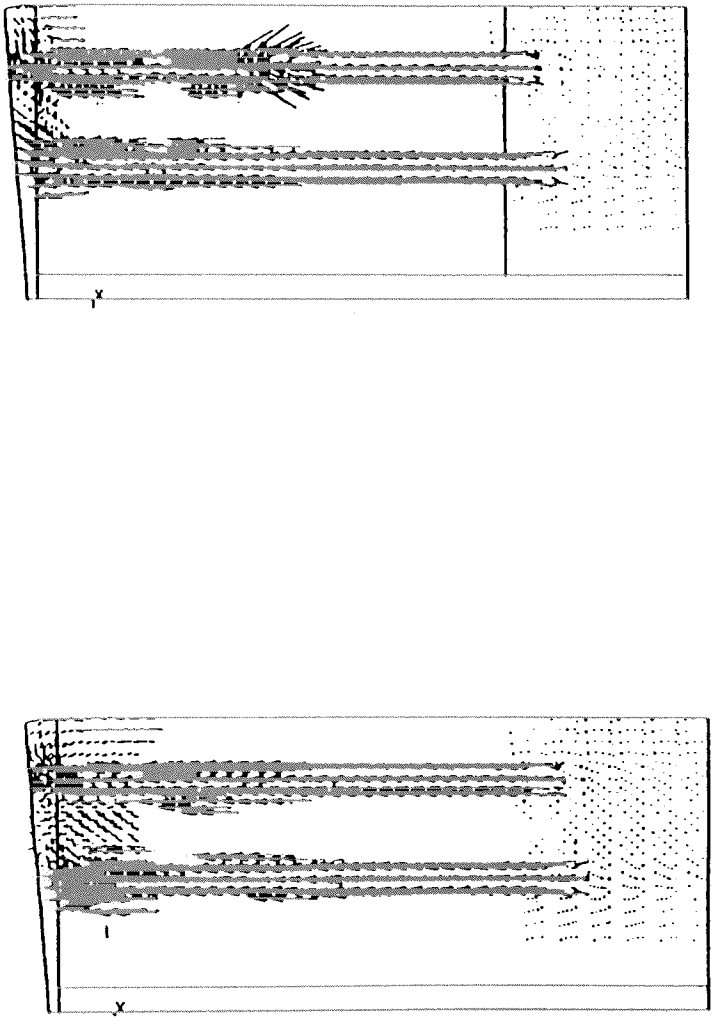

Fig. 3.7.6 Flow field at different times during the injection process.

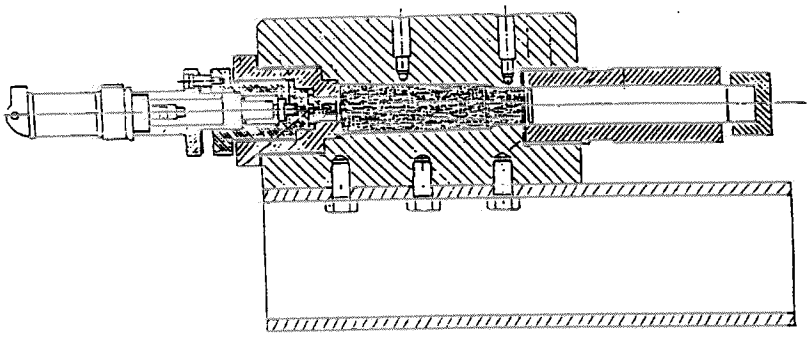

Fig. 3.8.1 Drawing of the BOFORS 30 mm gun.

Fig. 3.8.2 Euler mesh for the 40 mm gun (partly).

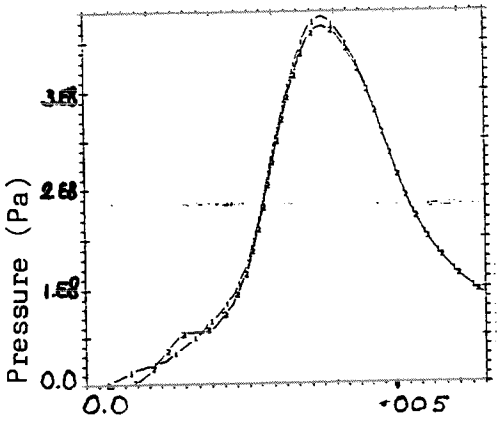

Fig. 3.8.3 Computed pressure history at the two transducers in the 40 mm gun.

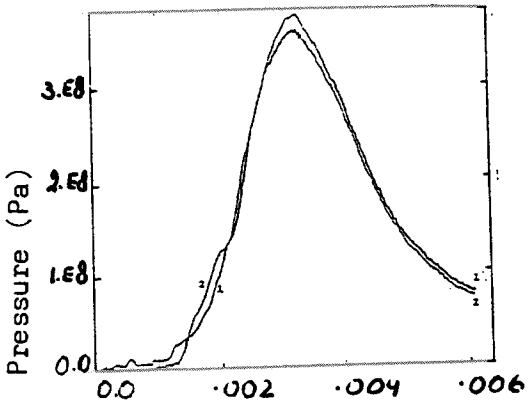

Fig. 3.8.4 Measured pressure history at the two transducers in the 40 mm gun.

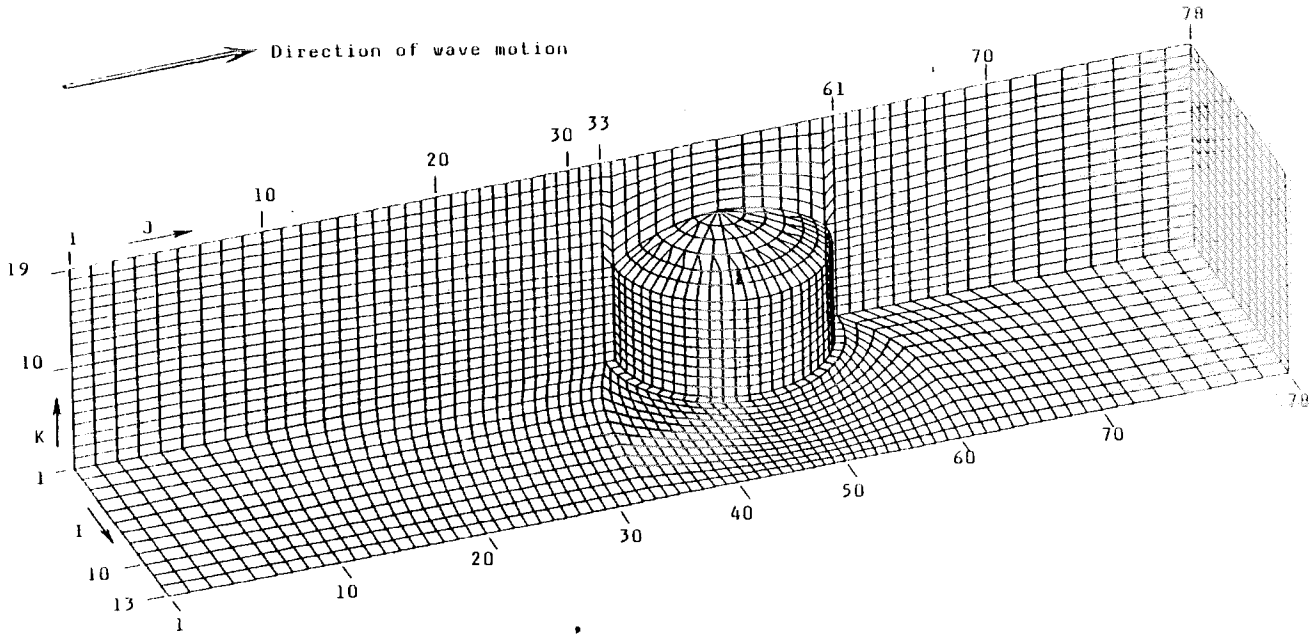

Fig. 3.9.1 Computational model (cut-away view).

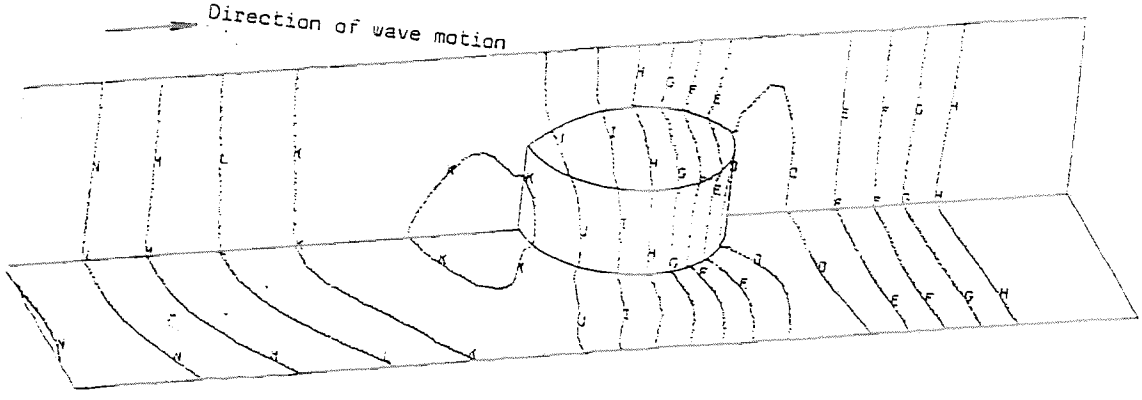

Fig. 3.9.2 Isobars after 400 msec.

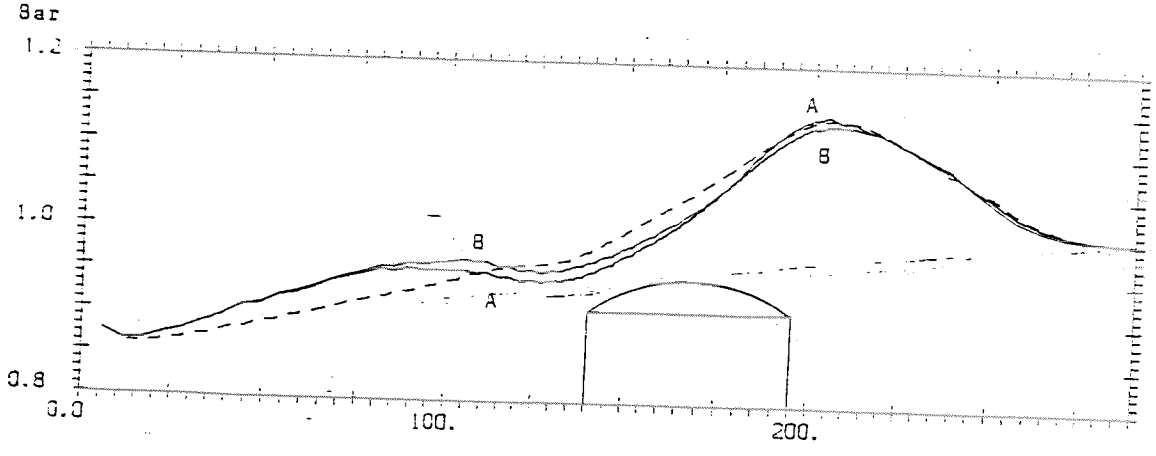

Fig. 3.9.3 Pressure frofiles along plane of symmetry at time 400 ms; A;ground Level; B; Level at top of tank wall; Dashed line; unobstructed flow.

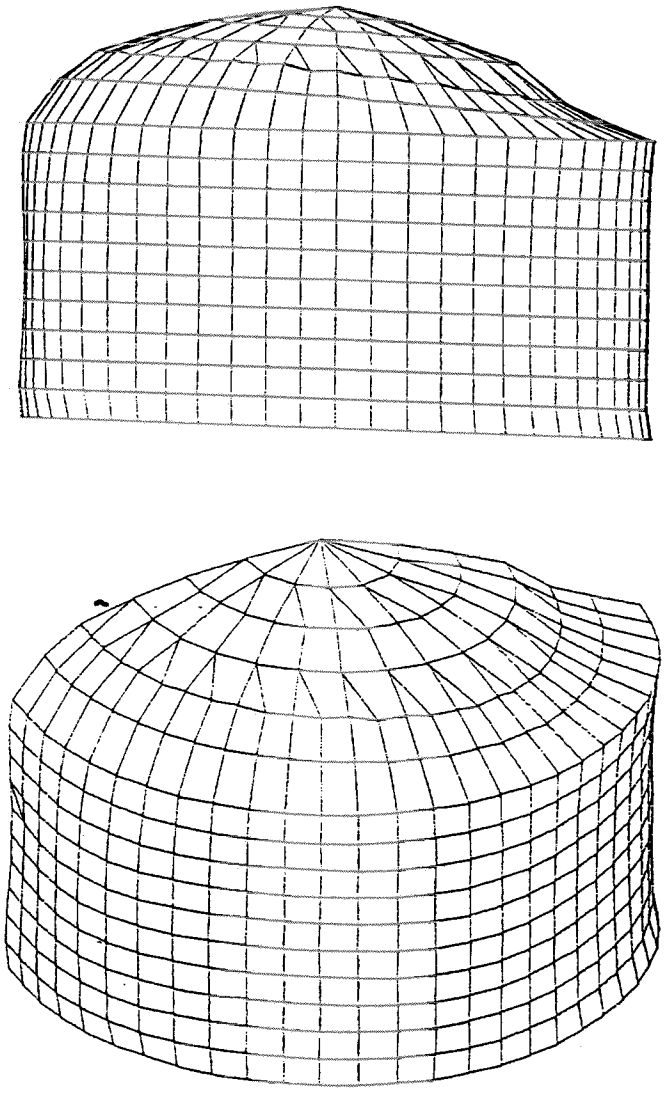

Fig. 3.9.4 Deformed shape of the tank at 400 msec (exagerated displacements).

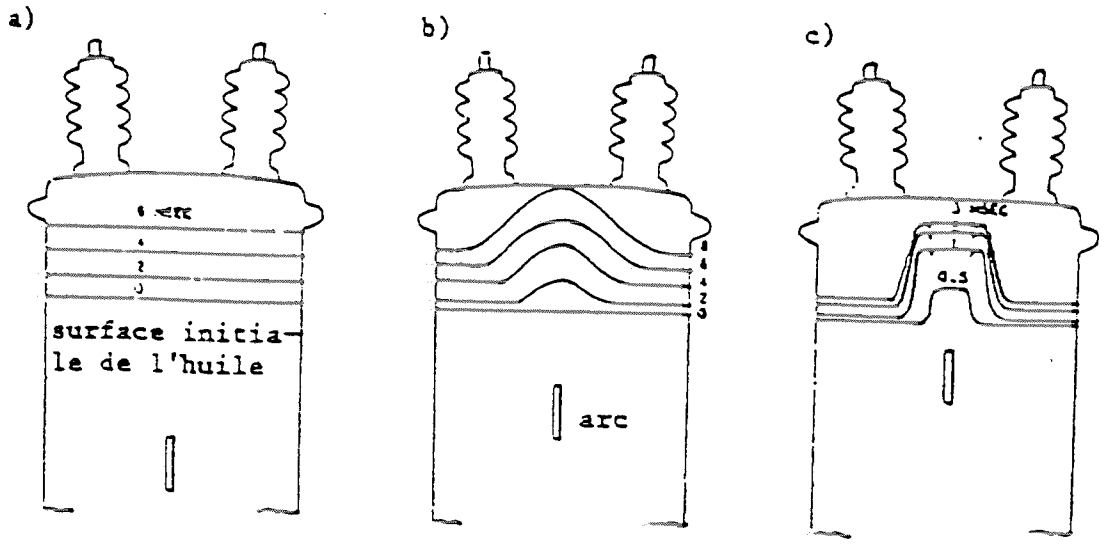

Fig. 3.10.1 OIL Piston domed surface surface breakthrough

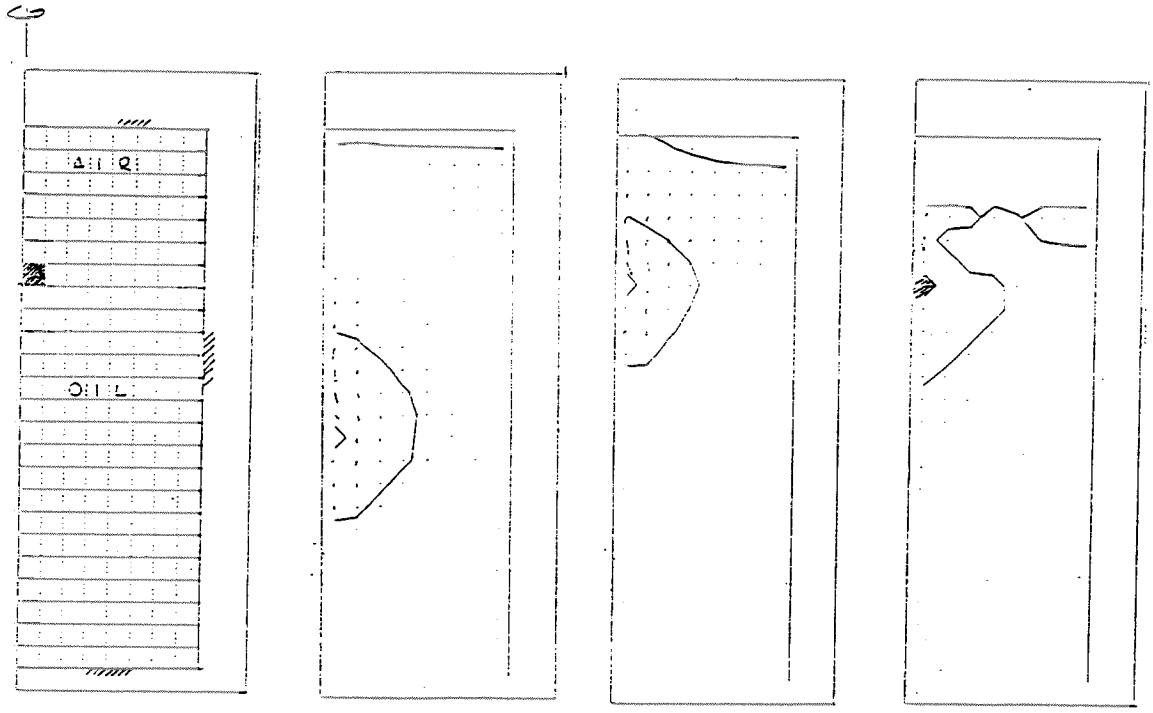

Fig. 3.10.2 Model OIL piston domed surface surface breakthrough